ENGINEERING

Electrically assisted 3D printing of nacre-inspired structures with self-sensing capability

Yang Yang[1], Xiangjia Li[1], Ming Chu[2], Haofan Sun[2], Jie Jin[1], Kunhao Yu[3], Qiming Wang[3], Qifa Zhou[4], Yong Chen[1,5]*

Lightweight and strong structural materials attract much attention due to their strategic applications in sports, transportation, aerospace, and biomedical industries. Nacre exhibits high strength and toughness from the brick-and-mortar–like structure. Here, we present a route to build nacre-inspired hierarchical structures with complex three-dimensional (3D) shapes by electrically assisted 3D printing. Graphene nanoplatelets (GNs) are aligned by the electric field (433 V/cm) during 3D printing and act as bricks with the polymer matrix in between as mortar. The 3D-printed nacre with aligned GNs (2 weight %) shows lightweight property (1.06 g/cm^3) while exhibiting comparable specific toughness and strength to the natural nacre. In addition, the 3D-printed lightweight smart armor with aligned GNs can sense its damage with a hesitated resistance change. This study highlights interesting possibilities for bioinspired structures, with integrated mechanical reinforcement and electrical self-sensing capabilities for biomedical applications, aerospace engineering, as well as military and sports armors.

INTRODUCTION

Lightweight and strong structural materials attract much attention due to their strategic applications in sports, transportation, construction, aerospace, and biomedical industries (*1*–*4*). In addition, multifunctional wearable sensors for health monitoring have attracted increasing attention (*5*, *6*). However, most developed piezoresistive sensors are soft and cannot protect the human body. A multifunctional wearable sensor with protective property is on demand for applications such as sports and military armors (*7*). Hierarchical structures in nacre lead to superior mechanical performance even with relatively weak constituents—adequately protecting its soft body (*8*). The secret of nacre's excellent protective performance lies in its sophisticated hierarchical "brick and mortar" (BM) architecture ranging from nanoscopic/microscopic to macroscopic levels (*9*, *10*). This outstanding property serves as the basis for the design of lightweight and strong armor by translating specific microstructural and interfacial structures (*11*, *12*). Recently, different types of nacre-inspired layered nanocomposites have been fabricated with inorganic additives, including glass flake, alumina flake, graphene, and graphene nanoplatelets (GNs) (*13*–*15*). Traditional bottom-up assembly processes, including vacuum filtration, spray coating, ice templating, and self-assembly, have been intensively studied to fabricate nacre-inspired structures (*1*, *11*, *16*, *17*). However, these methods are focused on two-dimensional (2D) thin-film fabrication (*15*, *18*, *19*) or simple shape bulk structures with improved mechanical properties (*17*, *20*, *21*). It is challenging to use these methods to construct complex 3D structures with enhanced multifunctional properties. Additive manufacturing (3D printing) could be a powerful tool to address this challenge and build bioinspired 3D structures with improved mechanical and electrical properties (*22*–*24*). The alignment of fillers in polymer composites has been studied because of their impressive strength-to-weight ratios, while the interface bonding between the polymer matrix and fillers still needs to be improved (*25*–*27*). Recently, 3D-printing methods using shear forces, magnetic field, and acoustic field have been developed to build reinforced composites with aligned fillers (refer to table S1) (*25*, *28*).

Here, we present an electrically assisted 3D-printing method using aligned GNs (aGNs) in the photocurable resin (G^+ from MakerJuice—notated as MJ) to build nacre-inspired hierarchical structures. The proposed fabrication procedure takes advantage of the nanoscale-to-microscale assembly induced by the electric field and the microscale-to-macroscale assembly by 3D printing. The 3D-printed hierarchical structures with aGNs show reinforced mechanical properties compared to those with random GNs (rGNs). The 3D-printed artificial nacre with aGNs displays comparable specific toughness and strength to the natural nacre. It also has an anisotropic electrical property, unlike the natural nacre. A smart helmet with both protective property and self-sensing capability can be fabricated using the electrically assisted 3D-printing process. The bioinspired BM architecture enhances the mechanical strength and electrical conduction by aligning GN in each layer to maximize their performance by crack deflection under loading. The electrically assisted 3D-printing method can build a multifunctional lightweight and strong 3D structure with electrically self-sensing capability.

RESULTS AND DISCUSSION

Electrically assisted 3D printing of nacre-inspired structures

Natural nacre has evolved unique microstructures composed of $CaCO_3$ platelets (~500 nm thick) acting as "bricks" and bonded by the protein "mortar" (~10 nm thick) in between (fig. S4) to enable predictable protection of its soft body (*2*, *29*, *30*). This BM structure plays a key role in the process of dissipating crack energy under loading through typical toughening mechanisms such as crack deflection, interlocking, and mineral bridging (*20*). Replicating nacre's structure is important as it sheds light on the design of tough engineering structures for protection; however, its fabrication is challenging because it is hierarchical, with features from nanoscale to macroscale. Previous attempts at 3D printing of nacre-inspired structures are emphasized on

[1]Epstein Department of Industrial and Systems Engineering, University of Southern California, 3715 McClintock Ave., Los Angeles, CA 90089, USA. [2]Department of Chemical Engineering and Materials Science, University of Southern California, 925 Bloom Walk, Los Angeles, CA 90089, USA. [3]Sonny Astani Department of Civil and Environmental Engineering, University of Southern California, Los Angeles, CA 90089, USA. [4]Department of Biomedical Engineering, University of Southern California, 1042 Downey Way, Los Angeles, CA 90089, USA. [5]Department of Aerospace and Mechanical Engineering, University of Southern California, 3650 McClintock Ave., Los Angeles, CA 90089, USA.
*Corresponding author. Email: yongchen@usc.edu

the shape mimicry and study of related reinforced mechanical properties (*25*, *26*, *31*).

Here, we developed an electrically assisted 3D-printing method to build an artificial nacre with hierarchical structures similar to those of the natural nacre. Using aGNs in the photocurable polymer, we show that this artificial nacre notably improved mechanical and electrical properties. The intrinsic toughening in the nacre's structure is primarily a result of crack deflection at the platelet interfaces (*11*). In this study, the GN with a thickness of 8 nm, a large surface area of 120 to 150 m^2/g, and a diameter of 25 μm was chosen to increase the interface area. GNs were further grafted with 3-aminopropyltriethoxysilane (3-APTES) to strengthen the interface and the load transfer between the polymer matrix and GNs (figs. S1 and S2). Figure 1A shows the setup of the electrically assisted 3D printing to build nacre-inspired structures using MJ/GNs composites (see Materials and Methods). The electric field (433 V/cm) was used to enable the alignment of GNs in the composite during the layer-based 3D-printing process. Two parallel plate electrodes were used with DC voltage to induce the parallel alignment (gaps, 3 cm; 1300 V; Fig. 1B). The alignment relaxation time is determined by

$$\tau^{-1} = (F(D)/3\eta)G \quad (1)$$

$G = \varepsilon_0 \varepsilon E^2/2$, where ε_0 is the electric permittivity of vacuum, η is the matrix viscosity, G is the rotational torque, ε is the anisotropic dielectric constant, and $F(D)$ is the shape factor including aspect ratio D (*22*). The equation shows that the relaxation time is proportional to the matrix viscosity. To reduce the time for GNs alignment, we used a photocurable resin (MJ) with low viscosity [90 centipoise (cP), 20°C]. When subjected to an electric field, GNs in a dielectric liquid are polarized and gain a dipole moment (μ) due to different dielectric properties and electrical conductivities between the inclusion and the liquid (*32*). 2D GNs have shape anisotropy. The polarization moment parallel to the platelet is much higher than that perpendicular to the platelet. The difference leads to the rotation of GN. The overall torque acting on the GN is the superposition of the torques induced by the electric fields that are parallel and perpendicular to its axis

$$T^e = \mu_{\parallel} \times E_{\perp} - \mu_{\perp} \times E_{\parallel} \quad (2)$$

and is resisted by the viscous torque from the liquid

$$T^v = -\eta\theta' k_r \quad (3)$$

(Fig. 1D), with $E_{\perp} = E \sin\theta$ and $E_{\parallel} = E \cos\theta$, where θ is the angle between the electric field direction and the semi-major axis of GN, η is the viscosity, θ′ is the angular velocity, and k_r is the rotational friction coefficient. Once rotated, polarized GNs tend to attract each

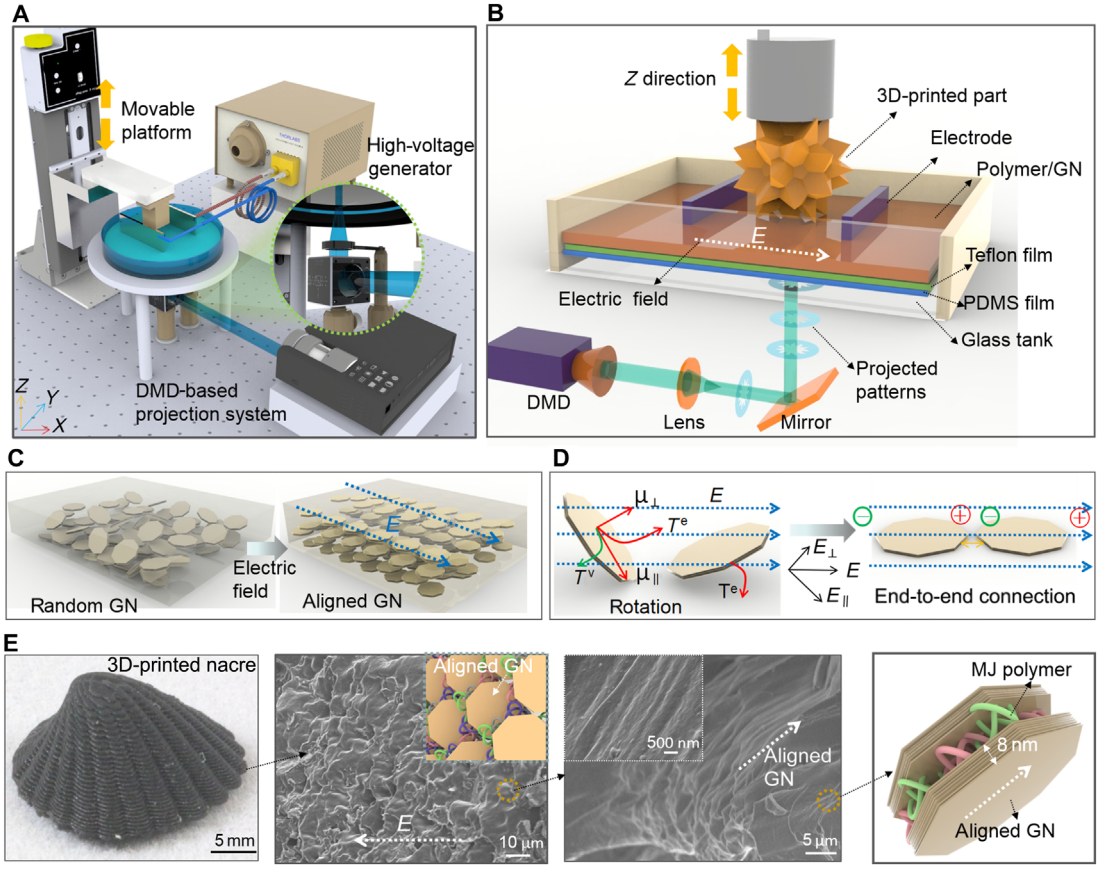

Fig. 1. Schematic diagram of the electrically assisted 3D-printing platform for the construction of nacre-inspired structures. (**A**) Diagram of the electrically assisted 3D-printing device. (**B**) Illustration of the bottom-up projection-based stereolithography process. (**C** and **D**) Schematic diagrams showing the alignment of GNs under the electric field and alignment mechanisms, respectively. (**E**) 3D-printed nacre with aGNs and SEM images showing surface and cross-section morphology. DMD, digital micromirror device; PDMS, polydimethylsiloxane.

other due to the opposite charges presented at their ends (Fig. 1D). The aGNs can be seen to be parallel, closely packed, and homogeneous throughout the sample layers due to the electric field (Fig. 1E and fig. S3). In each layer, GN bricks are separated by the polymer matrix in between that acts as mortar. All these structural features are critical for the excellent mechanical performance of the 3D-printed nacre. The GN not only have outstanding intrinsic properties but also are geometrically compatible with lamellae in the natural nacre's BM structure. Because the GN exhibit high in-plane rigidity and substantial out-of-plane flexibility, their strengthening efficiency in nanocomposites is strongly affected by their arrangement (*29*). Specifically, the aGNs will carry most of the load in the composite when the alignment is parallel to the load. The images in Fig. 1E and the microscopic images in fig. S5B show that the nacre model is successfully built with a layer thickness of 100 μm, with aGNs stacking within each layer. Comparisons highlight the strong similarities between the 3D-printed nacre and the natural nacre in their macroscale morphology and the microscale structure (fig. S4 and Fig. 1E). Specifically, the microscale structure of the 3D-printed nacre was characterized by a dense stacking of lamellae, in which the 2D GNs and the polymer matrix alternately stack (Fig. 1E). The polymer matrix between the aGNs acts as a sandwich-like structure similar to the sandwich-like $CaCO_3$ chitin structure in biogenic nacre (fig. S4). The inorganic GN sheets act as bricks, while the MJ polymer serves as the mortar between aGNs in the 3D-printed nacre.

Investigation of toughing mechanisms

The stress-strain curve of the natural nacre demonstrates an interesting behavior with several peaks for energy dissipation (Fig. 2C). The natural nacre demonstrates its ability to channel nonlinear deformation and suppresses crack growth through crack deflection and branching (Fig. 2, D and E) (*33*). Within the natural nacre's hierarchical structure, toughening mechanisms at multiple length scales have been proposed to contribute to the marked improvement in mechanical performance. In comparison, the stress-strain curve of the 3D-printed nacre with aGNs shows similar behavior to that of the natural nacre (Fig. 2F). The laminated structure in the 3D-printed nacre leads to crack branching, crack deflection (Fig. 2, G and H), and nanoplatelet bridging (Fig. 3E), similar to those of the natural nacre (*21*, *34*). Because of its unique BM structure, crack deflection up to millimeter length was found in the 3D-printed nacre (Fig. 2G). This deflection is considered to be the primary energy-dissipating

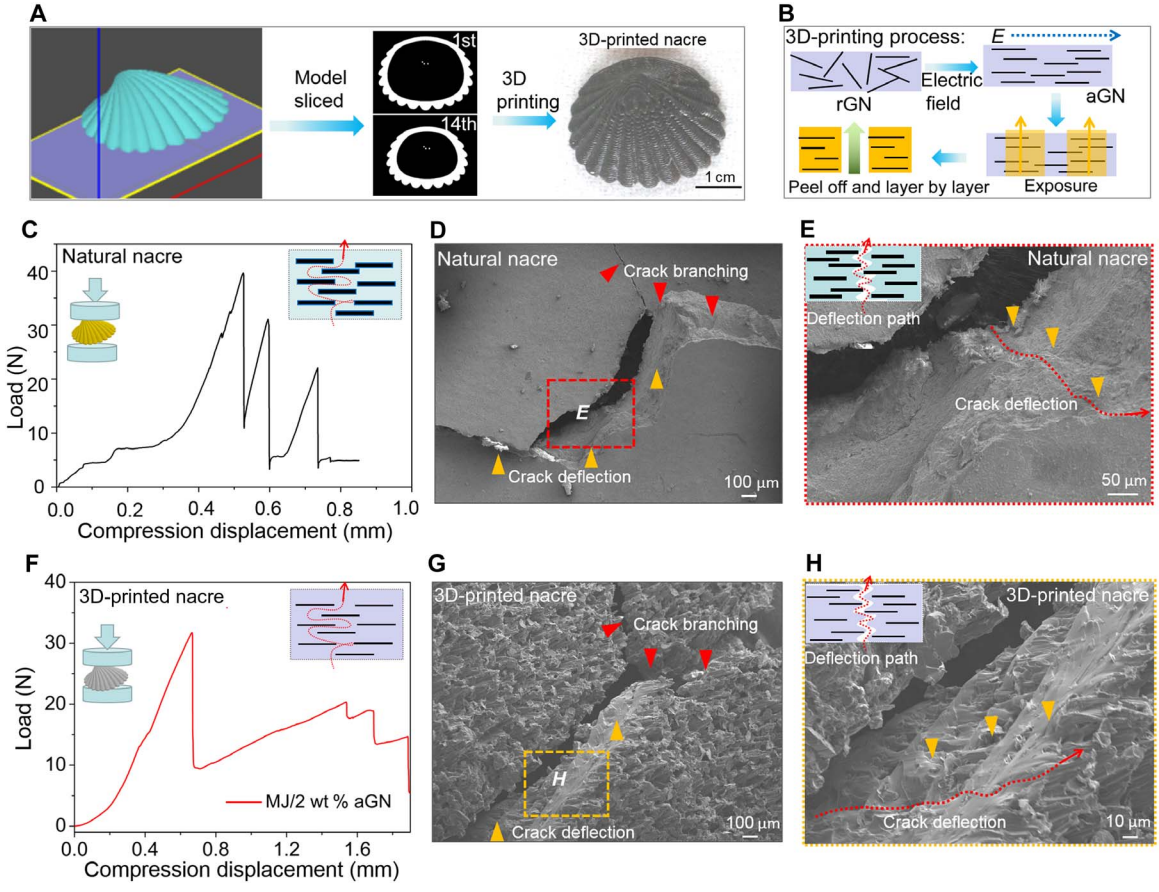

Fig. 2. The 3D-printing process. (**A**) Nacre model by SolidWorks (from Dassault Systèmes), sliced using our DMD-based stereolithography software to generate projection patterns. (**B**) rGNs are aligned by the electric field (blue dotted arrow shows the direction) to generate aGNs during the 3D-printing process; after the alignment, the composites solidify after light exposure (yellow part), the alignment of GNs is kept in the composites, and then the build plate peels after the layer is complete to print additional layers with aGNs. (**C**) Compression of natural nacre and SEM images of the fracture surface, showing crack deflection (yellow arrowheads) and crack branching (red arrowheads) in (**D**) and crack deflection between layers in (**E**). (**F**) 3D-printed nacre with 2 wt % aGNs under loading with crack deflection and branching in (**G**). (**H**) SEM image showing deflection between layers (yellow arrowheads).

mechanism in the natural nacre (*2*, *16*). A detailed structural analysis to understand the intrinsic factors that lead to the improved mechanical property of the artificial nacre is discussed in the remaining sections.

We compared the stress-strain behavior of the 3D-printed nacre with rGNs and aGNs for different mass ratios of GNs (Fig. 3A). The stress-strain curves of the 3D-printed nacre with rGNs show a sharp drop behavior (Fig. 3A) and typical brittle fractures with crack propagation, as compared to those of the natural nacre (Fig. 3B). Structural simulation using COMSOL Multiphysics demonstrates that the stress is concentrated on the joint area between rGNs and the polymer matrix within cracks (Fig. 3C). This inhomogeneous stress distribution can easily pull out rGNs (Fig. 3B, inset) and leads to a catastrophic failure. The pullout of the rGNs occurs at lower stress, resulting in markedly less energy dissipation and an early failure. The maximum load (the load at failure) shows that there is an increment for composites with aGNs compared with rGNs for the same load (Fig. 3D). This demonstrates that the alignment of GNs in the artificial nacre plays a critical role in crack deflection and energy dissipation. The maximum load reaches a maximum value with 2 weight % (wt %) aGNs. The decrease of the maximum load with a loading of 2.5 wt % GNs is due to the aggregation of nanoplatelets (see fig. S2). The aGNs sheets were observed to act as bridges between cracks owing to strong interactions between the aGNs and the polymer matrix (Fig. 3E). In particular, the edges of aGNs are curved rather than flattened, indicating that the breakage of the covalent bonds between the polymer matrix and the GN brings the deformation of aGNs (Fig. 3E). The structural simulation shows that the aGNs bridges lead to the homogeneous stress distribution on the joint area between the aGNs and the polymer matrix; hence, aGNs can carry loads that would otherwise be used to promote macroscopic crack advancement (Fig. 3F) (*30*, *35*–*37*). With the further increase of loading, the energy dissipation that is required to break the resulting aGNs bridges leads to ductile-phase toughening (*38*). Natural materials, such as bamboo, wood, and bone, have unique mechanical properties that usually depend on synergistic effects from interfacial interactions and multiscale building blocks (*2*, *39*). Similarly, hydrogen bonding networks and π-π interaction are formed between GNs and the two monomers in the MJ photocurable resin (epoxy diacrylate and glycol diacrylate) (fig. S8) (*40*). Similar to the interlock between adjacent platelets in the natural nacre, the Si-O-Si groups act as covalent bonding sites to promote the interlock between adjacent GNs (fig. S1) (*41*). Covalent bonding, hydrogen bonding, π-π interaction, and aGNs bridging usually synergistically work together in enhancing mechanical properties, resulting in an amplification effect (*42*). The synergistic effect leads to crack branching, crack deflection, and multiple peaks in the load-compression displacement curves for the composites with aGNs. Accordingly, because of the control of the structural architecture at the microscale and macroscale levels, we have combined a number of toughening mechanisms operating over a broad range of dimensions to generate extensive crack tip shielding and fracture resistance. Therefore, this unique BM structure constructed by electrically assisted 3D printing presents a type of lightweight, strong, and tough materials that can be used to fabricate arbitrary 3D geometric shapes.

The standard three-point bending tests were performed to measure the toughness of the 3D-printed composites with rGNs, aGNs, and a reference sample using the pure polymer (samples size, 25 mm × 5 mm × 5 mm; notch depth, 3 mm). The results show that the pure polymer sample exhibits a purely linear elastic response until a catastrophic failure occurs. The corresponding fracture surface shows no crack

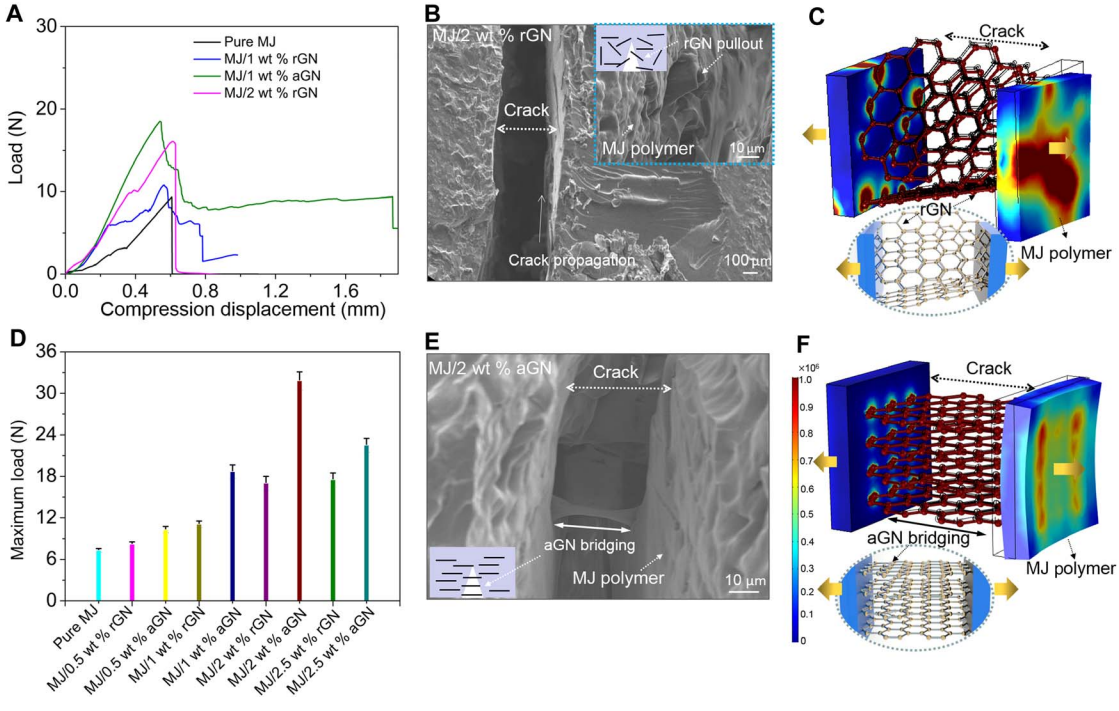

Fig. 3. Mechanical property and microstructure study of 3D-printed nacre. (**A**) Comparison of compression properties of the 3D-printed nacre with different loadings and alignments. (**B**) Crack propagation in MJ/rGNs nacre with the breaking of rGNs. (**C** and **F**) Simulations of stress distribution of MJ/rGNs and MJ/aGNs by COMSOL Multiphysics, respectively. (**D**) Comparison of maximum compression load for the 3D-printed nacre with different mass ratios of GNs. (**E**) Crack deflection of MJ/aGNs nacre and bridging and interlocking of aGNs.

deflection (Fig. 4A). With rGNs in the 3D-printed sample, progressive failure occurs because of stable crack propagation (Fig. 4B) and the related increment of fracture toughness (Fig. 4D). In comparison, after the alignment of GNs, we obtain a stable crack arrest and deflection by the toughening of brick-like platelets, similar to that of the natural nacre (Fig. 4C). Crack propagation is deflected by aGNs and suppressed by aGNs bridging with a subsequent curving during crack growth. Thus, energy dissipation is synergistically enhanced by these crack suppression mechanisms, leading to a higher toughness. Simulation using COMSOL Multiphysics reveals that the damage in MJ/aGNs composites not only localizes at the crack tip but also is widely distributed ahead of the growing crack by deflecting microcracks (Fig. 4I). Instead of the unstable (catastrophic) cracking characteristic of the MJ/rGNs composites (Fig. 4H), the primary characteristic of nacre-inspired MJ/aGNs composites is its extrinsic toughening mechanism, which provides the means to induce stable (subcritical) crack growth (Fig. 4I) (*43*). aGNs-related bridging and interlocking also translate to an increase in dissipated energy and toughening, which contribute to the composite's outstanding crack arrest performance.

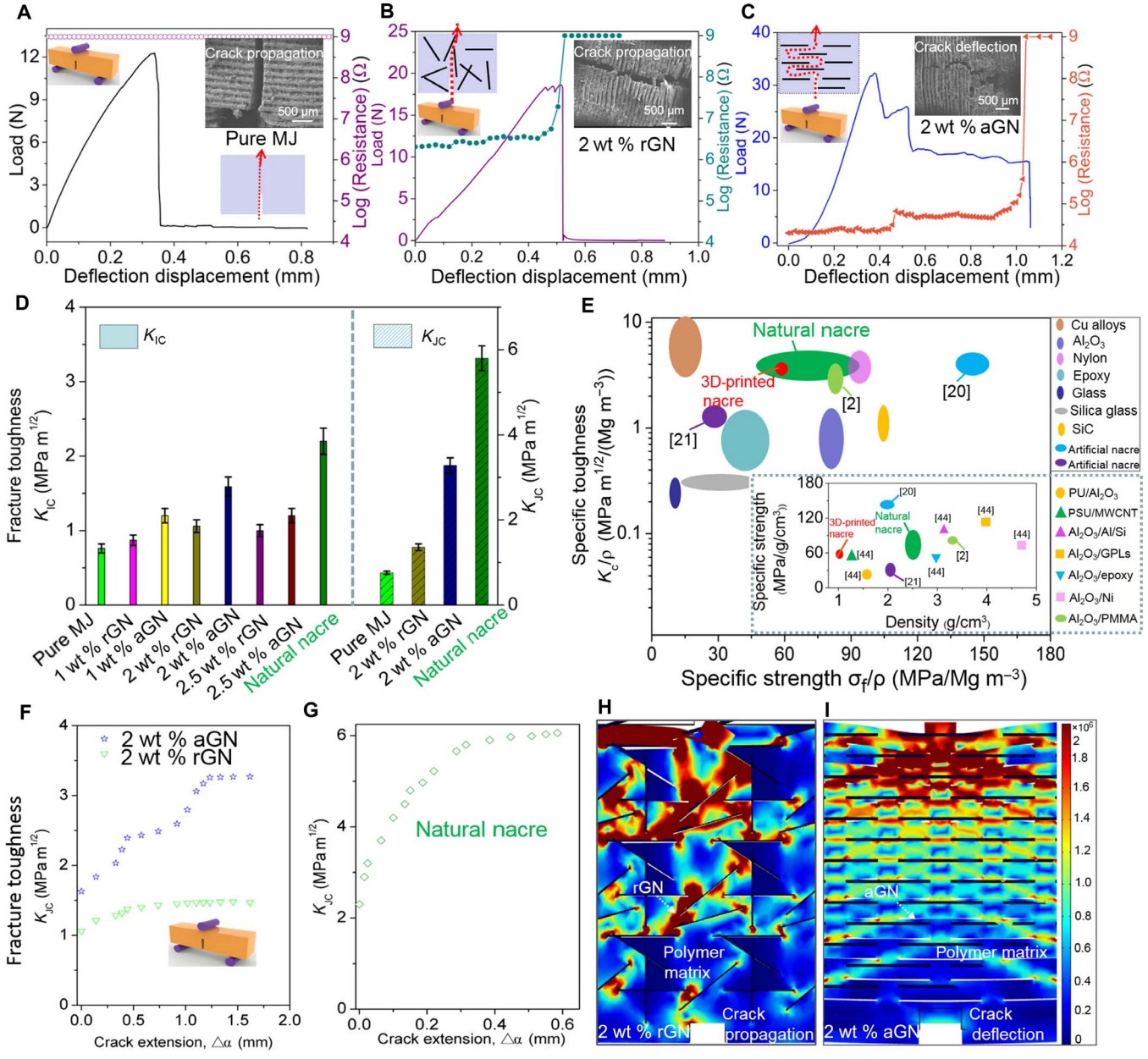

Fig. 4. Comparison of fracture toughness by three-point bending test. (**A** to **C**) Compression force versus resistance change for pure MJ, MJ/2 wt % rGNs, and MJ/2 wt % aGNs, respectively (with inset SEM images showing the related fracture surfaces). (**D**) Comparison of fracture toughness for crack initiation (K_{IC}) and stable crack propagation (K_{JC}) of the 3D-printed nacre with the natural nacre. (**E**) Comparison of specific toughness and specific strength of the 3D-printed nacre with others' work (inset shows the specific strength with density for various nacre-inspired composites). *R*-curves of the 3D-printed nacre (**F**) and the natural nacre (**G**). Simulations of stress distribution by COMSOL Multiphysics for the 3D-printed nacre with rGNs (**H**) and aGNs (**I**).

The capability of a material with preexisting cracks to resist fracture is defined as fracture toughness and is a critical mechanical property of interest because it determines structural integrity and reliability (*20*). The fracture toughness for crack initiation K_{IC} (describing the resistance to crack initiation) is significantly higher for aGNs than for rGNs with the same loading (Fig. 4D). The tests show that the K_{IC} of nanocomposites with 2 wt % [1.06 volume % (vol %)] aGNs has the highest value (1.59 MPa $m^{1/2}$) and is increased by 115% compared with the pure polymer. However, this value is still lower than that of the natural *Cristaria plicata* nacre (~2.4 MPa $m^{1/2}$) (*20*). With the further increase of filler loading, the fracture toughness decreases for both rGNs and aGNs due to the aggregation of GNs. The fracture toughness for stable crack propagation K_{JC} of the 3D-printed nacre with aGNs increases by 109% from the crack initiation (~1.59 MPa $m^{1/2}$) to the end of the stable crack propagation (~3.28 MPa $m^{1/2}$) (E = 3.5 GPa), which far exceeds those of the pure MJ bulk (~0.79 MPa $m^{1/2}$) and the rGNs composite (~1.33 MPa $m^{1/2}$) but is still lower than that of the natural *C. plicata* nacre (~5.9 MPa $m^{1/2}$) (Fig. 4D) (*20*). However, our 3D-printed nacre is more lightweight than the natural nacre [ρ_1 = 1.06 g/cm^3 for our 3D-printed nacre and ρ_2 = 2.58 g/cm^3 for the natural nacre (*20*)]. Consequently, both the specific toughness and the specific strength of the 3D-printed nacre are comparable with those of the natural nacre (Fig. 4E). Our 3D-printed nacre has the lowest density compared with other nacre-inspired composites (inset image in Fig. 4E and table S2) (*44*). For natural materials, fracture resistance increases with crack extension, generating a characteristic rising crack resistance curve (*R*-curve) (*2*, *11*, *45*). The *J*-*R* curve approach was applied to quantitatively study the changes of K_{JC} with the crack extension (Δa) (*46*, *47*). The results show that the 3D-printed nacre exhibits an extensive rising *R*-curve behavior (Fig. 4F) similar to that of the natural *C. plicata* nacre (Fig. 4G) [copyright from (*20*)], indicating their resistance to fracture during the crack growth. It is noted that there is no *R*-curve for the 3D-printed structure with the rGNs composite due to crack propagation (Fig. 4F). The *R*-curve behavior gives us a better understanding of how the aGNs in the nanocomposite can sustain subcritical cracking, thus delaying or even inhibiting the catastrophic failures, which is critical for developing engineering structures with high toughness and self-sensing capability. These results strongly illustrate that the lightweight 3D-printed nacre with aGNs exhibits high toughness due to the multiscale replication of the hierarchical BM structure from the natural nacre.

Investigation of anisotropic electrical properties for self-sensing

Different from the natural nacre, our 3D-printed nacre shows a significantly improved electrical conductivity that can be useful for applications requiring self-sensing property (e.g., sports and military armors). The piezoresistive responses of MJ/rGNs and MJ/aGNs composites were studied. Figure 5A shows that the light-emitting diode (LED) is "on" in the direction parallel to the GNs alignment but is "off" in the direction perpendicular to the alignment for the 3D-printed nacre with aGNs. The resistance of the composite with aGNs is 10^2 times lower in the direction that is parallel to the alignment than that with aGNs in the perpendicular direction and the composite with rGNs (Fig. 5B). The anisotropic electrical property is attributed to the fast electron transport parallel to the alignment direction between adjacent aGNs but is blocked by the insulated polymer matrix in the direction that is perpendicular to the alignment (Fig. 5C) (*15*, *42*). A wearable helmet designed for a Lego bicycle rider was 3D-printed to study its self-sensing capability (Fig. 5D) (Materials and Methods). Compared with rGNs, the helmet with aGNs shows both improved impact and compression resistances. The drop-tower impact test shows that the helmet with rGNs was totally broken, while the helmet with aGNs still kept its shape (fig. S11). Note that the helmet with aGNs (0.36 g) can sustain the impact of an iron ball 305 times its weight (110 g). After the impact, the brightness of LED connected to the helmet slightly decreased because of the crack formation and increased resistance (fig. S11C). We constructed an RC circuit and used an RC time function provided by the microcontroller to measure the resistance changes of the 3D-printed helmet during the impact and compression tests (Fig. 5G and fig. S13). For the helmet with rGNs, the LED was always off due to the large resistance (Fig. 5E). In comparison, for the helmet with aGNs, the LED was turned on due to the structure's much smaller resistance. During compression, the brightness of the LED decreased because of the crack formation and deflection. Last, the LED went off after a catastrophic failure of the helmet (Fig. 5F). The measured resistance change related to the applied load for the helmet with rGNs is shown in Fig. 5H. Note a sharp increase on the helmet's resistance (from blue zone to red zone) when the catastrophic failure occurs. This is attributed to crack propagation and pullout of the rGNs during the catastrophic failure (Fig. 3F). Without the electron transport between adjacent GNs the resistance of the helmet will markedly increase after failure. Hence, the failure of the 3D-printed helmet with rGNs would happen instantly, and the LED was kept off and showed no alarm to the structural failure (movie S1). In comparison, the 3D-printed helmet with aGNs reveals quite a different behavior during the compression test. The stress-strain curve shows several peaks due to the crack deflection by aGNs, demonstrating energy dissipation during compression (Fig. 5I). Meanwhile, aGNs bridging between cracks keeps the electron transport with a slight increase of resistance (yellow zone in Fig. 5I), which corresponds to the decrease of the LED's brightness (Fig. 5F). With the further increase of loading, the resistance increases markedly due to the catastrophic failure (red zone in Fig. 5I). Hence, the existence of the yellow zone and the related brightness change demonstrate crack formation and deflection, acting as an alarm for the self-sensing behavior of the smart helmet with aGNs (movie S2). Besides, the helmet with aGNs shows over 10^2 times higher resistance change after catastrophic failure compared to the one with rGNs (fig. S14). Hence, the nacre-inspired nano-laminated architecture provides extrinsic toughening and enhancement of electrical conductivity by aligning GNs in the nanocomposites (*19*). With the mass customization capability of the 3D-printing technology, 3D-printed smart structures that are lightweight and strong could find more potential applications in biomedical, aerospace, military, and sports industries.

CONCLUSION

In summary, the lessons learned from the natural nacre provide key ideas to build multifunctional structures with high toughness. An electrically assisted 3D-printing process using aGNs in the polymer matrix has been developed to fabricate complex 3D structures with a hierarchical nacre-inspired BM architecture. The 3D-printed structure with aGNs shows significantly enhanced toughness, impact, and compression resistances due to the synergistic effect and crack

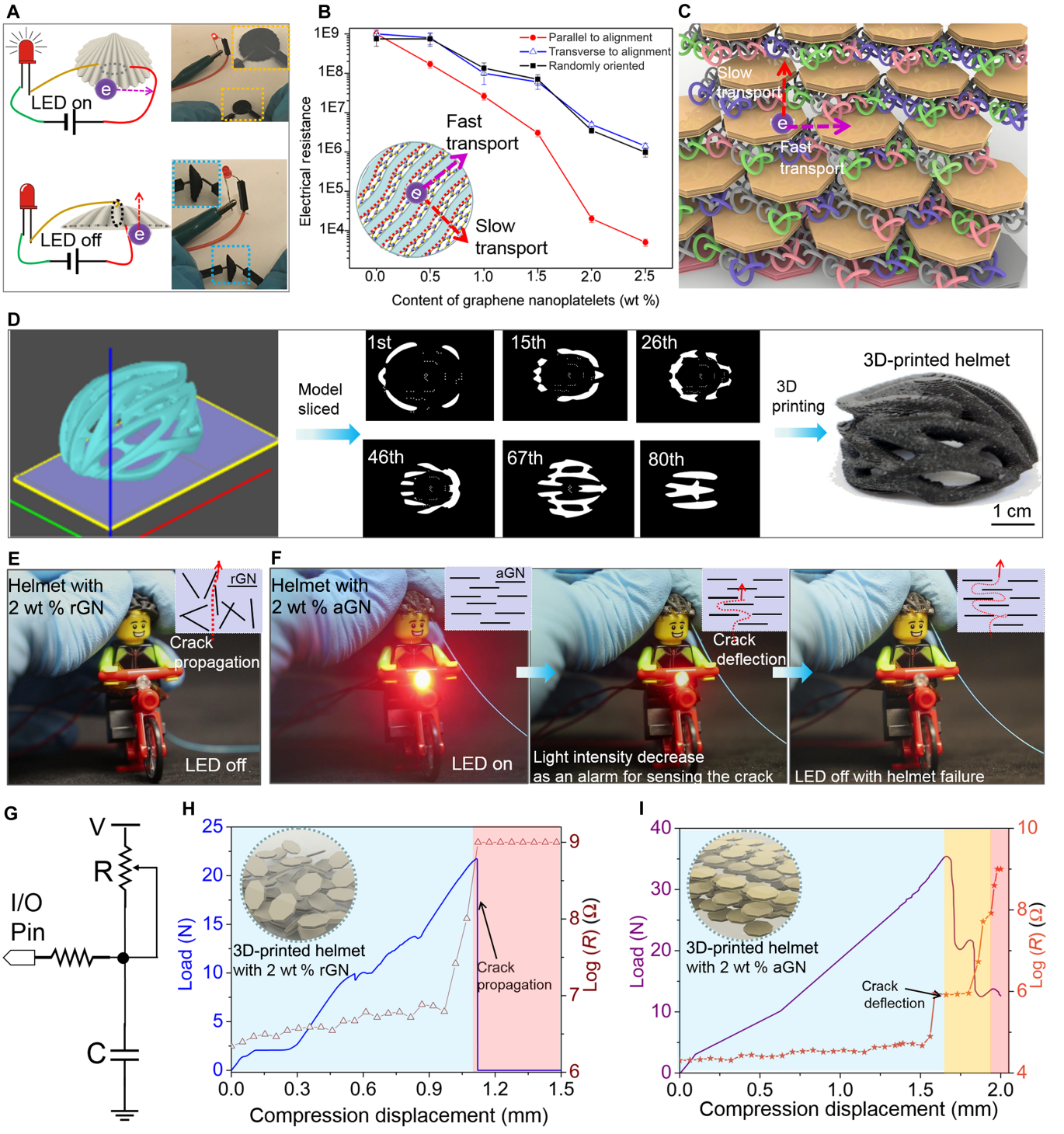

Fig. 5. 3D-printed smart helmet with anisotropic electrical property. (**A**) Anisotropic electrical property of the 3D-printed nacre. (**B**) Changes of electrical resistance with different GNs loadings and alignments. (**C**) Schematic diagram showing the layered polymer/GNs structure with anisotropic electrical resistance. (**D**) 3D-printing process of a self-sensing smart helmet. Demonstration of the wearable sensor on a Lego bicycle rider showing different self-sensing properties for the 3D-printed helmets with rGNs (**E**) and aGNs (**F**). (**G**) Circuit design for the tests. Compression force of the 3D-printed helmets with related compression displacements and resistance changes for rGNs (**H**) and aGNs (**I**), respectively. (Photo credit: Yang Yang, Epstein Department of Industrial and Systems Engineering, University of Southern California.)

deflection. The 3D-printed nacre displays lightweight property with comparable specific fracture toughness to the natural nacre. In addition, the alignment of GNs leads to the anisotropic electrical property, presenting a feasible direction for building protective wearable sensors that can self-sense the crack. The 3D-printed smart helmet can protect the human body and sense its potential damage. This study shows that the alignment of GN creates the bridge and interlock, which is essential to confer the stress-induced damage in

the 3D-printed structure. The developed electrically assisted 3D-printing process can fabricate structures with excellent integrated mechanical and electrical properties as well as complex 3D shapes. Such a new fabrication technique could enable the design and fabrication of the smart structures that are lightweight yet strong for various potential applications in biomedical, aerospace, transportation, sports, and military industries.

MATERIALS AND METHODS

Surface modification of GN

GNs (0.5 g; surface area, 120 to 150 m^2/g; 25 μm; Sigma-Aldrich) was first chemically treated with 30 ml of 10 N sulfuric acids in the presence of 1 g of potassium dichromate for 1 hour at 80°C. It was then filtered and washed with hot and cold water several times to remove chromic acid and dried in an oven at 90°C. Then, 0.5 ml of 3-APTES dissolved in acetone was added to the GN dispersed in water, and the mixture was stirred for 1 hour at 80°C. The resultant was filtered and washed with acetone (fig. S1A).

Preparation of MJ/GNs composite resin

The photocurable resin G+ (MakerJuice Labs, KS, USA) was selected in our study due to its excellent mechanical property and low viscosity. It contains high tensile epoxy diacrylate (≈9000 psi) and glycol diacrylate as well as the photoinitiator. This particular resin has a tensile strength of 63 MPa. The surface-modified GN powder was mixed with the polymer resin for 2 hours under magnetic stirring and then ultrasonic bath for 30 min. We degassed the composite in the vacuum before fabrication. Different mass ratios of GNs were used [0.5 wt %, 1 wt %, 1.5 wt %, 2 wt % (1.06 vol %), and 2.5 wt %] to study the related mechanical properties.

We applied DC voltages using a high-voltage power supply (model 210-30R, Spellman, NY, USA). Fourier transform infrared spectroscopy (FTIR) spectra were collected using an FT/IR 420 Fourier transform infrared spectrometer. The optical images were obtained using a Micro-Vu Sol 161 microscope. Scanning electron microscopy (SEM) images of the fracture cross section of the printed nacre model were taken using a JSM-7001F microscope.

Electrically assisted 3D printing of artificial nacre

The MJ/GNs nanocomposite was deposited in a transparent glass tank (Fig. 1A); the photocurable resin was cured after mask images were projected upward onto the bottom of the substrate via the optical system. Two parallel plate electrodes (1 cm × 3 cm) were used with DC voltages to obtain the parallel alignment. The nacre model was first created using SolidWorks and then sliced with an in-house–developed "digital micromirror device (DMD)–based stereolithography" software to generate different patterns (Fig. 2A). Mask images of the computed patterns were then projected on the resin surface to build different layers (Fig. 2A, the number in the figure shows the number of layers). The electrically assisted 3D-printing process aligned and selectively polymerized programmed parts to have specific reinforcement orientation within each layer. After the layer was fabricated and attached to the previous layer, it was peeled off from the Teflon film on the tank to print additional layers (Fig. 2B). For example, the first layer was built by projecting the first pattern and the process was repeated until the 56th layer was obtained. For the fabrication process, different patterns can be projected on the surface of the MJ/GNs nanocomposite. The composites solidified because of the photocurable property of the resin, and the alignment of GNs in each layer was fixed after a portion of the composites was solidified. After the first layer was cured on the base, the base was moved up and then moved down for the second layer to be cured and so on. Uniform thin layers were then recoated by moving the platform to form the desired gap between the previously cured layers and the glass substrate. In this case, the electric field guided the alignment of GNs in the MJ resin before the photocuring process. The resolution of the DMD chip (Texas Instruments, Dallas, TX) was 1024 × 768, and the output light intensity of the projection system was 3.16 mW cm^{-2}.

Electrically assisted 3D printing of smart helmet

The helmet model was first created using SolidWorks and then sliced with the DMD-based stereolithography software system to generate different mask patterns (Fig. 5D). The patterns were then projected to build different 2D layers. A total of 87 layers were constructed to create the smart helmet. During the printing process, a DC voltage was applied to align GNs in the MJ/GNs nanocomposite to build the helmet model. The electrical and mechanical properties of the 3D-printed smart helmet were tested after the fabrication and removal of the part from the base. A Keithley 2400 sourcemeter was used to measure the resistance of the 3D-printed nacre and helmet. In all the tests, five samples with the same alignment and loading of GNs were fabricated and tested to reduce experimental error.

Mechanical testing

The mechanical properties of the natural nacre, the 3D-printed nacre, and the helmet were measured using a universal testing machine (Instron 5492 Dual Column Testing Systems, Instron, MA, USA). Before the test, the sample was put in the middle of the test plate, with the compression force vertical to the alignment of GN. For the compression test, the static compression was chosen, and the velocity of compression was 1 mm min^{-1} with a maximum compression distance of 2 mm. For the three-point bending test, the velocity of compression was 1 mm min^{-1} with a maximum compression distance of 1.5 mm. The pictures from the side view were instantly taken using an optical microscope after the test. A multimeter was connected to the sample during the three-point bending and compression tests to record the resistance changes. For the single-edge notched bend (SENB) tests, samples with a thickness of 5 mm and a notch depth of 3 mm were 3D-printed. Fracture toughness for crack initiation K_{IC} was calculated using the following equations (*20*, *48*)

$$K_{IC} = \frac{P_{IC}S}{BW^{3/2}} f(a/W) \tag{4}$$

$$f(a/W) = \frac{3(a/W)^{1/2}[1.99 - (a/W)(1 - a/W)(2.15 - 3.93a/W + (a/W)^2)]}{2(1 + 2a/W)(1 - a/W)^{3/2}} \tag{5}$$

where P_{IC} is the maximum load in the SENB test, S is the support span (2.1 cm), B is the thickness of the specimen (5 mm), W is the width (5 mm), and a is the notch depth (3 mm).

Fracture toughness for stable crack propagation, K_{JC}, in this work was calculated from the elastic and plastic contribution, which relates to the J-integral calculation (*20*). The related equation is $J = J_{el} + J_{pl}$, where J_{el} is the elastic contribution based on linear elastic fracture

mechanics $J_{el} = \frac{K_{IC}^2}{E'}$. The plastic contribution J_{pl} can be calculated with the following equation

$$J_{pl} = \frac{2A_{pl}}{B(W-a)} \quad (6)$$

where A_{pl} is the plastic area underneath the load-displacement curve. Thus, J values can be transformed into K values by the following equation

$$K_{JC} = (JE')^{1/2} \quad (7)$$

where $E' = E(1-\nu)^2$, E is Young's modulus, and ν is the Poisson's ratio. As the variation of E influences K_{JC} in a limited way, E' can be replaced by E.

The crack extension Δa was calculated according to the previously reported indirect method with the following equation (*20*, *43*)

$$a_n = a_{n-1} + \frac{W-a_{n-1}}{2}\frac{C_n - C_{n-1}}{C_n}, C_n = u_n/f_n, \Delta a = a_n - a \quad (8)$$

where a_n and C_n are the crack length and complaisance, respectively, calculated at each point after the departure of the crack. u_n and f_n are the displacement and force at each point after the departure of the crack, respectively. W is the width of the specimen. In all the mechanical tests, five samples with the same alignment and loading of GNs were tested to reduce experimental error.

Simulation by COMSOL Multiphysics

The stress distributions of rGNs and aGNs within the crack were simulated by importing the model built from SolidWorks into COMSOL Multiphysics. A force (200 N) was applied to the model to study the deformation of the two models. The modulus of MJ was set to 300 MPa, and the modulus of GN was set to 1000 GPa.

SUPPLEMENTARY MATERIALS

Supplementary material for this article is available at http://advances.sciencemag.org/cgi/content/full/5/4/eaau9490/DC1

Supplementary Discussion

Fig. S1. Surface modification of GN and FTIR spectrum results.

Fig. S2. SEM images of fracture surfaces of the pure MJ polymer and MJ/GNs composites with rGNs and aGNs without and with surface modification, respectively.

Fig. S3. Schematic diagram and optical microscopic images show the alignment of GNs under the electric field.

Fig. S4. Picture of the natural nacre and SEM images.

Fig. S5. Sliced patterns of nacre model and SEM results of the 3D-printed nacre.

Fig. S6. Comparison of fracture surfaces of the natural nacre with the 3D-printed nacre.

Fig. S7. Changes of cure depth with the fraction of GNs.

Fig. S8. Demonstration of the bonding between the MJ polymer matrix and GN fillers.

Fig. S9. Crack deflection and the brick-and-mortar structure in the natural nacre and the 3D-printed nacre.

Fig. S10. A comparison of fracture behavior of the 3D-printed nacre and the natural nacre.

Fig. S11. The schematic diagram shows the drop-tower impact test setup for 3D printed helmet with rGNs and aGNs.

Fig. S12. The standard three-point bending tests were performed to study the flexural strength of the 3D-printed structures.

Fig. S13. The setup to test the resistance change of the 3D-printed helmet during compression.

Fig. S14. A comparison of the resistance changes of the 3D-printed helmets with different loadings of rGNs and aGNs during compression.

Fig. S15. Illustration of the microstructure of the 3D-printed nacre with rGNs and aGNs.

Fig. S16. The calculation of the interconnection of GNs in 3D-printed structures.

Table S1. Comparison of alignment of fillers in polymer-based composites using different methods.

Table S2. Comparison of densities, shape complexity, and electrical conductivity of nacre-inspired structures fabricated using different methods.

Movie S1. Self-sensing capability of 3D-printed helmet with rGNs.

Movie S2. Self-sensing capability of 3D-printed smart helmet with aGNs.

References (*49*–*60*)

REFERENCES AND NOTES

1. L. J. Bonderer, A. R. Studart, L. J. Gauckler, Bioinspired design and assembly of platelet reinforced polymer films. *Science* **319**, 1069–1073 (2008).
2. E. Munch, M. E. Launey, D. H. Alsem, E. Saiz, A. P. Tomsia, R. O. Ritchie, Tough, bio-inspired hybrid materials. *Science* **322**, 1516–1520 (2008).
3. U. G. K. Wegst, H. Bai, E. Saiz, A. P. Tomsia, R. O. Ritchie, Bioinspired structural materials. *Nat. Mater.* **14**, 23–36 (2015).
4. A. R. Studart, Towards high-performance bioinspired composites. *Adv. Mater.* **24**, 5024–5044 (2012).
5. Y. Yamamoto, S. Harada, D. Yamamoto, W. Honda, T. Arie, S. Akita, K. Takei, Printed multifunctional flexible device with an integrated motion sensor for health care monitoring. *Sci. Adv.* **2**, e1601473 (2016).
6. S. Yao, P. Swetha, Y. Zhu, Nanomaterial-enabled wearable sensors for healthcare. *Adv. Healthc. Mater.* **7**, 1700889 (2018).
7. S. Choi, H. Lee, R. Ghaffari, T. Hyeon, D.-H. Kim, Recent advances in flexible and stretchable bio-electronic devices integrated with nanomaterials. *Adv. Mater.* **28**, 4203–4218 (2016).
8. H. D. Espinosa, A. L. Juster, F. J. Latourte, O. Y. Loh, D. Gregoire, P. D. Zavattieri, Tablet-level origin of toughening in abalone shells and translation to synthetic composite materials. *Nat. Commun.* **2**, 173 (2011).
9. H. Bai, Y. Chen, B. Delattre, A. P. Tomsia, R. O. Ritchie, Bioinspired large-scale aligned porous materials assembled with dual temperature gradients. *Sci. Adv.* **1**, e1500849 (2015).
10. M. A. Meyers, J. McKittrick, P.-Y. Chen, Structural biological materials: Critical mechanics-materials connections. *Science* **339**, 773–779 (2013).
11. F. Bouville, E. Maire, S. Meille, B. Van de Moortèle, A. J. Stevenson, S. Deville, Strong, tough and stiff bioinspired ceramics from brittle constituents. *Nat. Mater.* **13**, 508–514 (2014).
12. F. Song, A. K. Soh, Y. L. Bai, Structural and mechanical properties of the organic matrix layers of nacre. *Biomaterials* **24**, 3623–3631 (2003).
13. H. Kakisawa, T. Sumitomo, R. Inoue, Y. Kagawa, Fabrication of nature-inspired bulk laminar composites by a powder processing. *Compos. Sci. Technol.* **70**, 161–166 (2010).
14. O. O. Ekiz, A. F. Dericioglu, H. Kakisawa, An efficient hybrid conventional method to fabricate nacre-like bulk nano-laminar composites. *Mater. Sci. Eng. C* **29**, 2050–2054 (2009).
15. Y.-Q. Li, T. Yu, T.-Y. Yang, L.-X. Zheng, K. Liao, Bio-inspired nacre-like composite films based on graphene with superior mechanical, electrical, and biocompatible properties. *Adv. Mater.* **24**, 3426–3431 (2012).
16. P. Podsiadlo, A. K. Kaushik, E. M. Arruda, A. M. Waas, B. S. Shim, J. Xu, H. Nandivada, B. G. Pumplin, J. Lahann, A. Ramamoorthy, N. A. Kotov, Ultrastrong and stiff layered polymer nanocomposites. *Science* **318**, 80–83 (2007).
17. A. Finnemore, P. Cunha, T. Shean, S. Vignolini, S. Guldin, M. Oyen, U. Steiner, Biomimetic layer-by-layer assembly of artificial nacre. *Nat. Commun.* **3**, 966 (2012).
18. Q. Cheng, M. Wu, M. Li, L. Jiang, Z. Tang, Ultratough artificial nacre based on conjugated cross-linked graphene oxide. *Angew. Chem.* **125**, 3838–3843 (2013).
19. S. Wan, Y. Li, J. Peng, H. Hu, Q. Cheng, L. Jiang, Synergistic toughening of graphene oxide–molybdenum disulfide–thermoplastic polyurethane ternary artificial nacre. *ACS Nano* **9**, 708–714 (2015).
20. H.-L. Gao, S.-M. Chen, L.-B. Mao, Z.-Q. Song, H.-B. Yao, H. Cölfen, X.-S. Luo, F. Zhang, Z. Pan, Y.-F. Meng, Y. Ni, S.-H. Yu, Mass production of bulk artificial nacre with excellent mechanical properties. *Nat. Commun.* **8**, 287 (2017).
21. L.-B. Mao, H.-L. Gao, H.-B. Yao, L. Liu, H. Cölfen, G. Liu, S.-M. Chen, S.-K. Li, Y.-X. Yan, Y.-Y. Liu, S.-H. Yu, Synthetic nacre by predesigned matrix-directed mineralization. *Science* **354**, 107–110 (2016).
22. Y. Yang, Z. Chen, X. Song, Z. Zhang, J. Zhang, K. K. Shung, Q. Zhou, Y. Chen, Biomimetic anisotropic reinforcement architectures by electrically assisted nanocomposite 3D printing. *Adv. Mater.* **29**, 1605750 (2017).
23. Y. Yang, X. Li, X. Zheng, Z. Chen, Q. Zhou, Y. Chen, 3D-printed biomimetic super-hydrophobic structure for microdroplet manipulation and oil/water separation. *Adv. Mater.* **30**, 1704912 (2018).
24. Y. Yang, X. Song, X. Li, Z. Chen, C. Zhou, Q. Zhou, Y. Chen, Recent progress in biomimetic additive manufacturing technology: From materials to functional structures. *Adv. Mater.* **30**, 1706539 (2018).

25. J. J. Martin, B. E. Fiore, R. M. Erb, Designing bioinspired composite reinforcement architectures via 3D magnetic printing. *Nat. Commun.* **6**, 8641 (2015).
26. D. Kokkinis, M. Schaffner, A. R. Studart, Multimaterial magnetically assisted 3D printing of composite materials. *Nat. Commun.* **6**, 8643 (2015).
27. H. Le Ferrand, F. Bouville, T. P. Niebel, A. R. Studart, Magnetically assisted slip casting of bioinspired heterogeneous composites. *Nat. Mater.* **14**, 1172–1179 (2015).
28. B. G. Compton, J. A. Lewis, 3D-printing of lightweight cellular composites. *Adv. Mater.* **26**, 5930–5935 (2014).
29. M. Cao, D.-B. Xiong, Z. Tan, G. Ji, B. Amin-Ahmadi, Q. Guo, G. Fan, C. Guo, Z. Li, D. Zhang, Aligning graphene in bulk copper: Nacre-inspired nanolaminated architecture coupled with in-situ processing for enhanced mechanical properties and high electrical conductivity. *Carbon* **117**, 65–74 (2017).
30. S. Mann, D. D. Archibald, J. M. Didymus, T. Douglas, B. R. Heywood, F. C. Meldrum, N. J. Reeves, Crystallization at inorganic-organic interfaces: Biominerals and biomimetic synthesis. *Science* **261**, 1286–1292 (1993).
31. C. S. Tiwary, S. Kishore, S. Sarkar, D. R. Mahapatra, P. M. Ajayan, K. Chattopadhyay, Morphogenesis and mechanostabilization of complex natural and 3D printed shapes. *Sci. Adv.* **1**, e1400052 (2015).
32. G. Kim, Y. M. Shkel, Polymeric composites tailored by electric field. *J. Mater. Res.* **19**, 1164–1174 (2004).
33. F. Barthelat, R. Rabiei, Toughness amplification in natural composites. *J. Mech. Phys. Solids* **59**, 829–840 (2011).
34. Y. Shao, H.-P. Zhao, X.-Q. Feng, H. Gao, Discontinuous crack-bridging model for fracture toughness analysis of nacre. *J. Mech. Phys. Solids* **60**, 1400–1419 (2012).
35. R. J. Young, M. Liu, I. A. Kinloch, S. Li, X. Zhao, C. Vallés, D. G. Papageorgiou, The mechanics of reinforcement of polymers by graphene nanoplatelets. *Compos. Sci. Technol.* **154**, 110–116 (2018).
36. L. Gong, I. A. Kinloch, R. J. Young, I. Riaz, R. Jalil, K. S. Novoselov, Interfacial stress transfer in a graphene monolayer nanocomposite. *Adv. Mater.* **22**, 2694–2697 (2010).
37. R. J. Young, I. A. Kinloch, L. Gong, K. S. Novoselov, The mechanics of graphene nanocomposites: A review. *Compos. Sci. Technol.* **72**, 1459–1476 (2012).
38. L. S. Sigl, P. A. Mataga, B. J. Dalgleish, R. M. McMeeking, A. G. Evans, On the toughness of brittle materials reinforced with a ductile phase. *Acta Metall.* **36**, 945–953 (1988).
39. F. Barthelat, Z. Yin, M. J. Buehler, Structure and mechanics of interfaces in biological materials. *Nat. Rev. Mater.* **1**, 16007 (2016).
40. S. Gong, H. Ni, L. Jiang, Q. Cheng, Learning from nature: Constructing high performance graphene-based nanocomposites. *Mater. Today* **20**, 210–219 (2017).
41. H. Roghani-Mamaqani, V. Haddadi-Asl, In-plane functionalizing graphene nanolayers with polystyrene by atom transfer radical polymerization: Grafting from hydroxyl groups. *Polym. Compos.* **35**, 386–395 (2014).
42. S. Wan, Y. Li, J. Mu, A. E. Aliev, S. Fang, N. A. Kotov, L. Jiang, Q. Cheng, R. H. Baughman, Sequentially bridged graphene sheets with high strength, toughness, and electrical conductivity. *Proc. Natl. Acad. Sci. U.S.A.* **115**, 5359–5364 (2018).
43. H. Bai, F. Walsh, B. Gludovatz, B. Delattre, C. Huang, Y. Chen, A. P. Tomsia, R. O. Ritchie, Bioinspired hydroxyapatite/poly (methyl methacrylate) composite with a nacre-mimetic architecture by a bidirectional freezing method. *Adv. Mater.* **28**, 50–56 (2016).
44. H. Zhao, Y. Yue, L. Guo, J. Wu, Y. Zhang, X. Li, S. Mao, X. Han, Cloning Nacre's 3D interlocking skeleton in engineering composites to achieve exceptional mechanical properties. *Adv. Mater.* **28**, 5099–5105 (2016).
45. Q. Cheng, C. Huang, A. P. Tomsia, Freeze casting for assembling bioinspired structural materials. *Adv. Mater.* **29**, 1703155 (2017).
46. H. Peterlik, P. Roschger, K. Klaushofer, P. Fratzl, From brittle to ductile fracture of bone. *Nat. Mater.* **5**, 52–55 (2006).
47. K. J. Koester, J. W. Ager III, R. O. Ritchie, The true toughness of human cortical bone measured with realistically short cracks. *Nat. Mater.* **7**, 672–677 (2008).
48. G. Dwivedi, K. Flynn, M. Resnick, S. Sampath, A. Gouldstone, Bioinspired hybrid materials from spray-formed ceramic templates. *Adv. Mater.* **27**, 3073–3078 (2015).
49. H. Zhao, Z. Zhou, H. Dong, L. Zhang, H. Chen, L. Hou, A facile method to align carbon nanotubes on polymeric membrane substrate. *Sci. Rep.* **3**, 3480 (2013).
50. Y. He, Z. Cao, L. Ma, Shear flow induced alignment of carbon nanotubes in natural rubber. *Int. J. Polym. Sci.* **2015**, 964723 (2015).
51. M. A. Correa-Duarte, M. Grzelczak, V. Salgueiriño-Maceira, M. Giersig, L. M. Liz-Marzán, M. Farle, K. Sierazdki, R. Diaz, Alignment of carbon nanotubes under low magnetic fields through attachment of magnetic nanoparticles. *J. Phys. Chem. B* **109**, 19060–19063 (2005).
52. E. Camponeschi, R. Vance, M. Al-Haik, H. Garmestani, R. Tannenbaum, Properties of carbon nanotube–polymer composites aligned in a magnetic field. *Carbon* **45**, 2037–2046 (2007).
53. P. A. Smith, C. D. Nordquist, T. N. Jackson, T. S. Mayer, B. R. Martin, J. Mbindyo, T. E. Mallouk, Electric-field assisted assembly and alignment of metallic nanowires. *Appl. Phys. Lett.* **77**, 1399 (2000).
54. C. Liedel, K. A. Schindler, M. J. Pavan, C. Lewin, C. W. Pester, M. Ruppel, V. S. Urban, R. Shenhar, A. Böker, Electric-field-induced alignment of block copolymer/nanoparticle blends. *Small* **9**, 3276–3281 (2013).
55. W. Cui, M. Li, J. Liu, B. Wang, C. Zhang, L. Jiang, Q. Cheng, A strong integrated strength and toughness artificial nacre based on dopamine cross-linked graphene oxide. *ACS Nano* **8**, 9511–9517 (2014).
56. A. M. Shanmugharaj, J. H. Bae, K. Y. Lee, W. H. Noh, S.-H. Lee, S. H. Ryu, Physical and chemical characteristics of multiwalled carbon nanotubes functionalized with aminosilane and its influence on the properties of natural rubber composites. *Compos. Sci. Technol.* **67**, 1813–1822 (2007).
57. J. Kathi, K.-Y. Rhee, J. H. Lee, Effect of chemical functionalization of multi-walled carbon nanotubes with 3-aminopropyltriethoxysilane on mechanical and morphological properties of epoxy nanocomposites. *Compos. Part A Appl. Sci. Manuf.* **40**, 800–809 (2009).
58. K. W. Putz, O. C. Compton, M. J. Palmeri, S. T. Nguyen, L. C. Brinson, High-nanofiller-content graphene oxide–polymer nanocomposites via vacuum-assisted self-assembly. *Adv. Funct. Mater.* **20**, 3322–3329 (2010).
59. A. E. Jakus, E. B. Secor, A. L. Rutz, S. W. Jordan, M. C. Hersam, R. N. Shah, Three-dimensional printing of high-content graphene scaffolds for electronic and biomedical applications. *ACS Nano* **9**, 4636–4648 (2015).
60. J. Sun, B. Bhushan, Hierarchical structure and mechanical properties of nacre: A review. *RSC Adv.* **2**, 7617–7632 (2012).

Acknowledgments

Funding: Y.C. is grateful for the financial support of the NSF (grant nos. CMMI 1663663 and CMMI 1151191) and USC's Epstein Institute. Q.W. acknowledged the funding support from the Air Force Office of Scientific Research Young Investigator Program (FA9550-18-1-0192, program manager: J. S. Tiley) and NSF (CMMI-1762567). **Author contributions:** Y.Y. and Y.C. conceived and designed experiments. Y.Y., M.C., and H.S. performed experiments, data collection, and analysis. Y.Y. and X.L. performed the simulation by COMSOL Multiphysics and test of SEM images. J.J. and K.Y. assisted in the device performance measurement. Y.Y and Y.C. wrote the manuscript. All authors discussed and commented on the manuscript. **Competing interests:** The authors declare that they have no competing interests. **Data and materials availability:** All data needed to evaluate the conclusions in the paper are present in the paper and/or the Supplementary Materials. Additional data related to this paper may be requested from the authors.

Submitted 31 July 2018
Accepted 13 February 2019
Published 5 April 2019
10.1126/sciadv.aau9490

Citation: Y. Yang, X. Li, M. Chu, H. Sun, J. Jin, K. Yu, Q. Wang, Q. Zhou, Y. Chen, Electrically assisted 3D printing of nacre-inspired structures with self-sensing capability. *Sci. Adv.* **5**, eaau9490 (2019).

Electrically assisted 3D printing of nacre-inspired structures with self-sensing capability

Yang Yang, Xiangjia Li, Ming Chu, Haofan Sun, Jie Jin, Kunhao Yu, Qiming Wang, Qifa Zhou and Yong Chen

Sci Adv **5** (4), eaau9490.
DOI: 10.1126/sciadv.aau9490

Science Advances
AAAS

advances.sciencemag.org/cgi/content/full/5/4/eaau9490/DC1

Supplementary Materials for

Electrically assisted 3D printing of nacre-inspired structures with self-sensing capability

Yang Yang, Xiangjia Li, Ming Chu, Haofan Sun, Jie Jin, Kunhao Yu, Qiming Wang, Qifa Zhou, Yong Chen*

*Corresponding author. Email: yongchen@usc.edu

Published 5 April 2019, *Sci. Adv.* **5**, eaau9490 (2018)
DOI: 10.1126/sciadv.aau9490

The PDF file includes:

Other Supplementary Material for this manuscript includes the following:

(available at advances.sciencemag.org/cgi/content/full/5/4/eaau9490/DC1)

Movie S1 (.avi format). Self-sensing capability of 3D-printed helmet with rGNs.
Movie S2 (.avi format). Self-sensing capability of 3D-printed smart helmet with aGNs.

Table S1. Comparison of alignment of fillers in polymer-based composites using different methods.

	Fillers in polymer composites	Experimental procedure	References
Shear force	Nano-clay platelets	3D extrusion printing	[28]
	carbon fibers, silicon carbide whiskers	shear force by fluid flow	[49]
	carbon nanotubes	shear force by peel off	[50]
Magnetic field	Al_2O_3@Fe_3O_4	low magnetic field (40mT) with decoration by magnetic nanoparticles	[25]
	CNTs @Fe_3O_4	low magnetic field of 20mT with decoration by magnetic nanoparticles	[51]
	Multi walled carbon nanotubes	high magnetic field (15T)	[52]
Electric field	Au nanowire	Electric field of 10^4 V/cm	[53]
	Gold nanoparticles	Electric field of 10^4 V/cm	[54]
	MWCNT-S	Electric field of 300V/cm, controllable rotating angle between aligning direction	[22]
	Graphene nanoplatelets	Electric field of 400V/cm	[our work]

Recently, various alignment methods have been used to fabricate reinforced composites with aligned fillers. The shear force is usually used for fiber alignment by extruding materials through a small nozzle [28, 49]. The shear force from the peel-off process will also make the alignment of fillers [50]. For the magnetic field alignment method, decoration of fillers with magnetic nanoparticles is necessary [25,51]; otherwise, the magnetic field has to be extremely high (e.g., 15T for pure MWCNT) [52]. This requirement leads to additional magnetic particles added to the materials, which may adversely influence their mechanical properties. In addition, the interface bonding between inorganic fillers and the organic matrix plays a crucial role in mechanical reinforcement of composites. The mask-image-projection-based stereolithography (MIP-SL) process used in our study possesses high dimensional accuracy and high fabrication speed. The controlled electric field has been widely used for the alignment of Au nanowire, gold nanoparticles, carbon nanotubes, etc. [53,54,22]. We presented here an electrically assisted 3D printing method based on the MIP-SL process to fabricate nacre-inspired composite with aligned graphene nanoplatelets (GNs). First, the surface modification of GN with chemical groups promotes the interface bonding and load transfer between inorganic fillers and the polymer matrix (discussed in fig. S1). It is noticed that when the loading of GNs is low (<2.5 wt%), the alignment of GNs is easily controlled by an electric field. But for a higher loading of

GNs, the electrical alignment method is difficult due to the high viscosity of nanocomposites. In comparison, the shear-force-based alignment method can work with the loading of fillers up to 60 vol%[59].

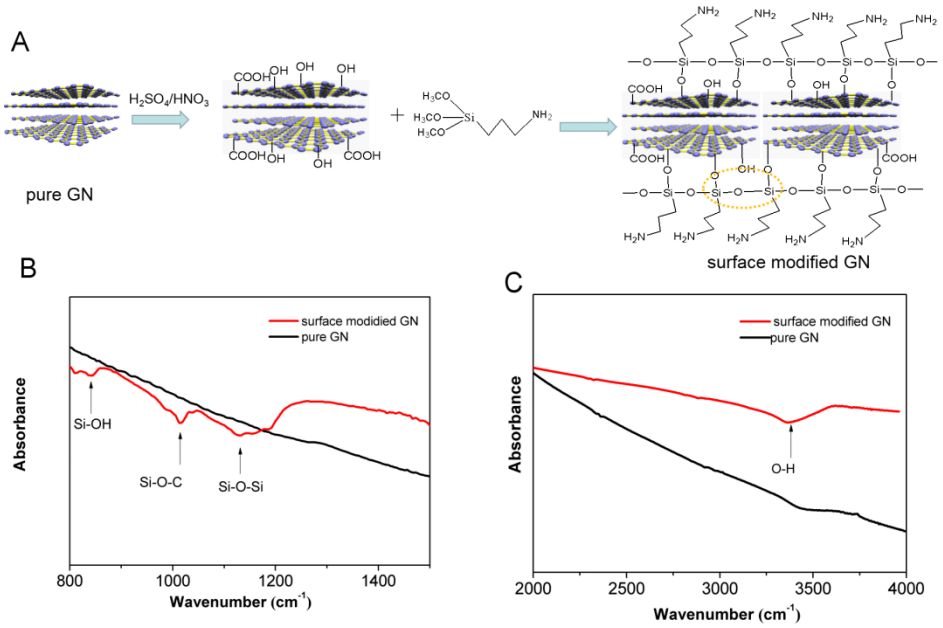

Fig. S1. Surface modification of GN and FTIR spectrum results. A) Representation of the surface modification procedure of GN; and (B, C) FTIR spectrum of pure GN and surface modified GN (S-GN).

In the current study, we did not change the direction of the electric field during the layer-by-layer fabrication process. It is because the Graphene nanoplatelets have the same in-plane orientation hence there is no need to change the electric field direction in the electrically assisted 3D printing process. Besides, the aligned $CaCO_3$ platelets in natural nacre do not change their in-plane orientations over layers [60]. However, the shifting of the electric field direction over layers can be easily realized by adding a rotation stage, which has been achieved in our previous study on the additive manufacturing of the 'Bouligand' patterned multiwalled carbon nanotubes (MWCNT) [22].

The comparison of the density, shape complexity and electrical conductivity of the nacre-inspired structures fabricated using different methods is listed in Table S2 [25,55,20,22,11,44]. The results demonstrate our 3D-printed nacre has excellent properties including low density, improved electrical conductivity as well as complex 3D geometric shapes.

Table S2. Comparison of densities, shape complexity, and electrical conductivity of the nacre-inspired structures fabricated using different methods.

Samples	Density (g/cm^3)	Shape complexity	Electrical conductive	References
3D printed nacre (MJ/2wt% *aGN)*	**1.06±0.02**	**controllable complex 3D shapes by 3D printing**	**Yes**	**Our work**
nacre-mimetic graphene oxide	1.6~1.8	2D thin film	Yes	[55]
nacre-mimetic magnetic aligned Al_2O_3	~1.6	controllable complex 3D shapes by magnetic 3D printing	No	[25
natural cristaria plicata nacre	2.58	natural nacre shape	No	[20
artificial nacre	1.73~1.83	simple bulk shape	No	[20]
synthetic nacre	2.18	simple bulk shape	No	[22]
PMMA/aluminia	2.52	simple bulk shape	No	[11]
Copper/Aluminia	3.96	simple bulk shape	No	[11]
nacre-mimetic aluminia	3.94	simple bulk shape	No	[11]
Al_2O_3/SWCNT	4.01	simple bulk shape	No	[44]
Al_2O_3/Ni	4.57	simple bulk shape	No	[44]
Al_2O_3/cyanate ester	1.87	simple bulk shape	No	[44]
Al_2O_3/epoxy	2.86	simple bulk shape	No	[44]

The interface bonding between the reinforced fillers and the polymer matrix is of great importance because it affects the load-transfer and energy exchange efficiency in composites. The surface modification of GN has been used to address the problem of low interfacial strength between interlayers of the artificial nacre. The surface modification of GN also allows the use of chemical bonding to improve the interfacial strength between adjacent layers. The schematic diagram shows the surface modification process of GN (fig. S1A) and is discussed in the experimental section. The FTIR spectra show that the hydroxyl group (3420cm^{-1}) is successfully bonded on the surface modified GN (S-GN). The reaction product S-GN shows clear absorption at 830cm^{-1} (Si-OH), 1080cm^{-1} (Si-O-C) and 1170cm^{-1} (Si-O-Si) [56,57]. These absorption bands characterize the presence of 3-aminopropyltriethoxysilane on the surface of S-GN (Supplementary materials, fig. S1A). The surface modified GN shows the alignment that is

parallel to the direction of the electric field under 433V/cm for 1 min (align for 30s and projection for 30s). The scanning electron microscope (SEM) images show that the surface modification improves the dispersity of GNs in the polymer resin (fig. S2D compared with S2E). The alignment keeps at a good level with the increment of loading up to 2 wt%, but loses its efficiency at 2.5 wt% because of the aggregation of nanoplatelets (fig. S2F). The aggregation of GNs will lead to defects in the 3D-printed composites and the related poor mechanical property. Figure S3 shows that the cure depth decreases with the increment of GNs loading (the cure depth was tested based on the set curing time of 30s). The projection time may be adjusted for different filler loadings.

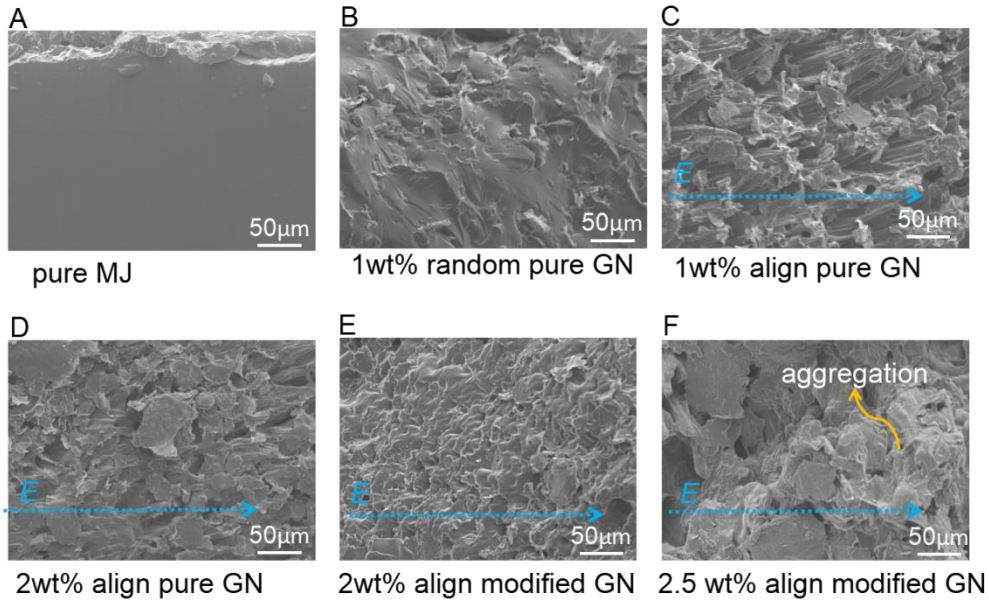

Fig. S2. SEM images of fracture surfaces of the pure MJ polymer and MJ/GNs composites with rGNs and aGNs without and with surface modification, respectively. (arrow shows the direction of applied electric field).

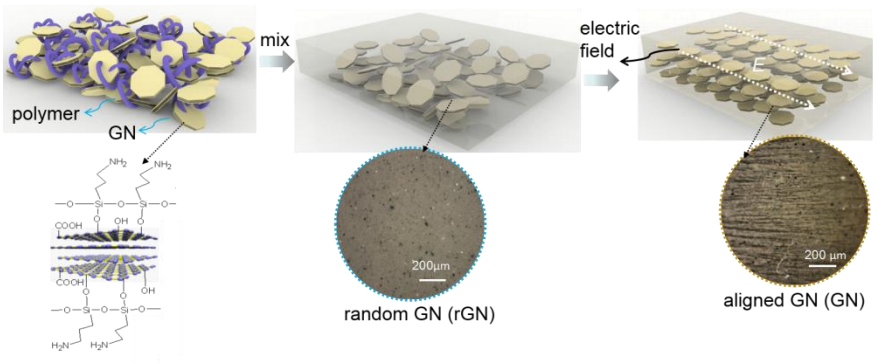

Fig. S3. Schematic diagram and optical microscopic images show the alignment of GNs under the electric field.

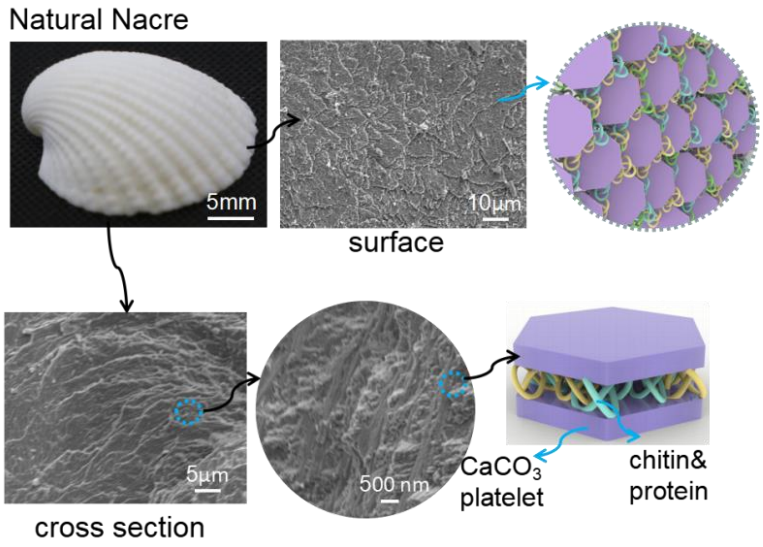

Fig. S4. Picture of the natural nacre and SEM images. The top and side views of SEM images of the natural nacre to show the 'brick and mortar structure' with aligned $CaCO_3$ platelets and chitin protein.

The uniformity of the layer thickness in the electrically assisted 3D printing process shows its good control of the 3D shapes in building reinforced architectures (fig. S5B). The SEM images show the interlayer bonding is strong in the layer-by-layer fabrication process with no defect found between adjacent layers.

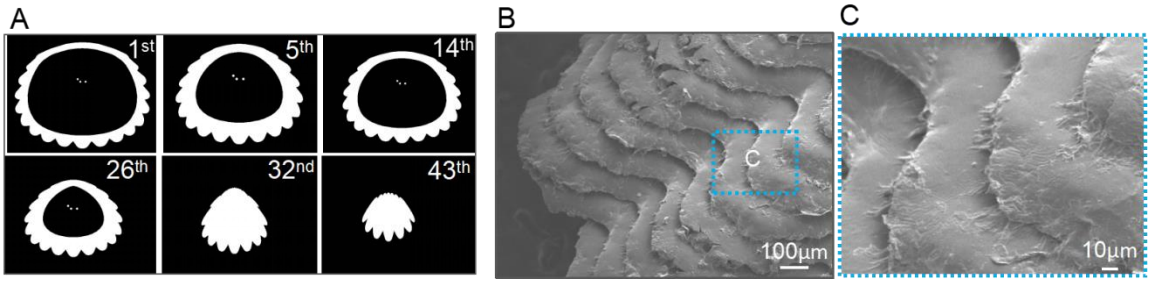

Fig. S5. Sliced patterns of nacre model and SEM results of the 3D-printed nacre. (A) the nacre model sliced in DMD-based Stereolithography software system to generate different patterns for layer fabrication; and (B, C) show SEM images of the 3D-printed nacre.

The fracture interface of the natural nacre is very rough and shows the brittle fracture behavior (fig. S6A). $CaCO_3$ platelets remain flattened owing to their brittleness after being pulled out (fig. S6A) [24]. The curved morphology of aGNs will absorb more energy during the shape changing, which leads to the increment of strain (Fig. 2C and 2F) [60]. When loaded, the aGNs sheets extensively slide against each other. The chemical bonding between aGNs sheets and polymer matrix will be stretched and broken along the sliding direction, resulting in the dissipation of a large amount of energy. When the loading is further increased, GN sheets are pulled out, which simultaneously results in stretching and curving behaviors (fig. S6B).

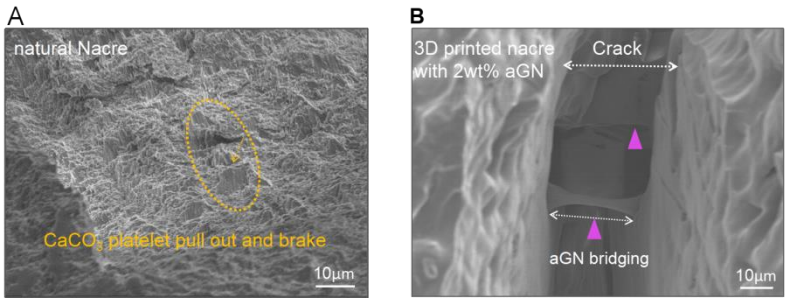

Fig. S6. Comparison of fracture surfaces of the natural nacre with the 3D-printed nacre. (A) SEM images show pull out $CaCO_3$ platelets at a crack in natural nacre; and (B) the aGNs bridging at a crack in the 3D-printed nacre with 2wt% aGNs.

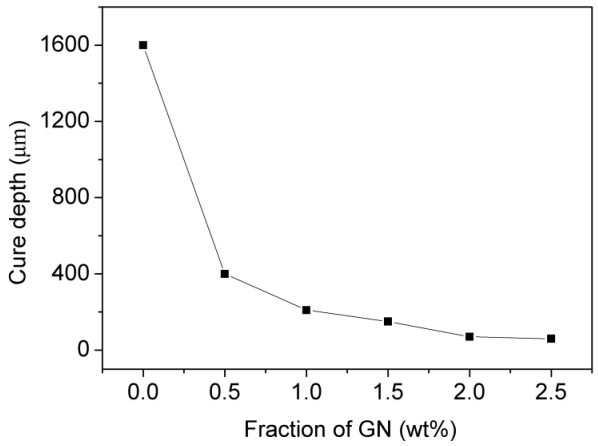

Fig. S7. Changes of cure depth with the fraction of GNs.

Figure S7 shows the decrease of cure depth with the increment of GN loading. The curing time was set as 30s in all of the tests. The resolution of the DMD chip (Texas Instrument, Dallas, TX) was 1024 × 768 and the output light intensity of the projection system was 3.16 mW cm^{-2}.

Weak hydrogen bonding exists in many natural materials. For example, the bone exhibits excellent fracture toughness due to the sacrificial hydrogen bonding between mineralized collagen fibrils [10]. Hydrogen bonding networks formed between GNs and oxygen groups on epoxy diacrylate and glycol diacrylate (two monomers in MJ photocurable resin) (fig. S8A). Different from the groups in Poly(methyl methacrylate) (PMMA) that can only act as a hydrogen bonding acceptor, the hydroxyl groups of epoxy diacrylate can serve as both hydrogen bonding acceptors and donors. Furthermore, the covalent C-C bonds in the epoxy diacrylate chain further link the hydrogen bonding into a multi-connected bridge, resulting in much stronger interface interactions [58]. The π-π interaction is also formed between oxygen-containing groups on GNs and aromatic regions with benzene rings in photocurable polymer [40] (fig. S8B). Meanwhile, the –Si–O end of APTES binds to GN and forms crosslink bonds with each other [41] (fig. S8C). Similar to the interlock between adjacent platelets in nacre, the Si-O-Si groups act as covalent bonding that promote the interlock between adjacent GNs. The synergistic effect from hydrogen bonding, π-π interaction, and covalent bonding between adjacent aGNs leads to high toughness [42]. The surface modification of GN leads to the chemical bonds on the surface which serves similar purposes as the mineral bridges in the natural nacre. Such bonding constrains

transverse expansion and promotes interfacial hardening, which further increases the energy dissipation. As the load continuously increases, the GNs sliding and transverse dilation happen. During the process, the interfacial hardening plays an important role when nanoplatelets slide. The interfacial bonding between GNs and the polymer matrix increases the load transfer and reduces the relative sliding [8]. The 3D-printed structure relies on a combination of mechanisms operating at different length scales to achieve high toughness. The synergy from the bioinspired nanolaminated architecture and the improved interfacial bonding leads to high mechanical toughness and ductility as well as the improved electrical conductivity in the polymer/aGNs composites.

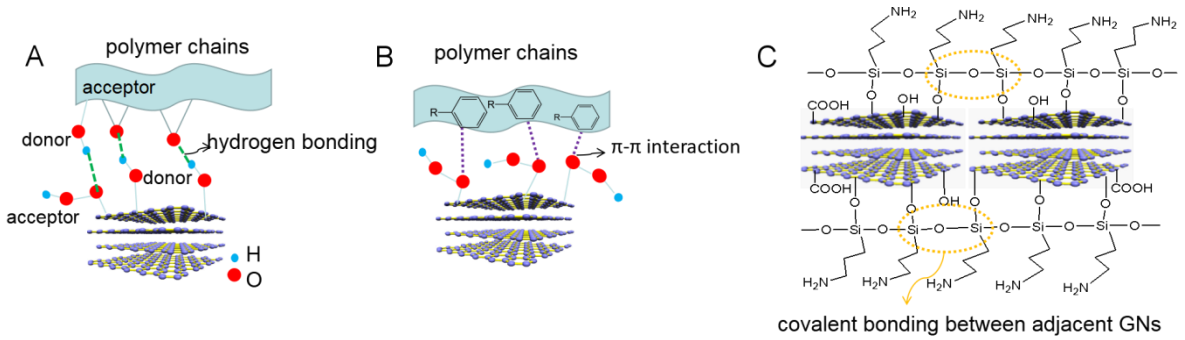

Fig. S8. Demonstration of the bonding between the MJ polymer matrix and GN fillers. Demonstration of (A) hydrogen bonding, (B) π-π interaction and (C) the covalent bonding between the MJ polymer matrix and GN fillers.

Similar to the natural nacre (fig. S9A), large-scale crack deflection generated by the aligned GNs and the enhanced interaction between layers greatly contribute to the improvement of the 3D-printed nacre's mechanical properties. At the microscale, graphene nanoplatelets are stacked like bricks by the alignment (fig. S9A), which is similar to the $CaCO_3$ platelets in the natural nacre (fig. S9B). The MJ polymer serves as the mortar that bonds aGNs together (fig. S9D), which is similar to the protein in the natural nacre (fig. S9B).

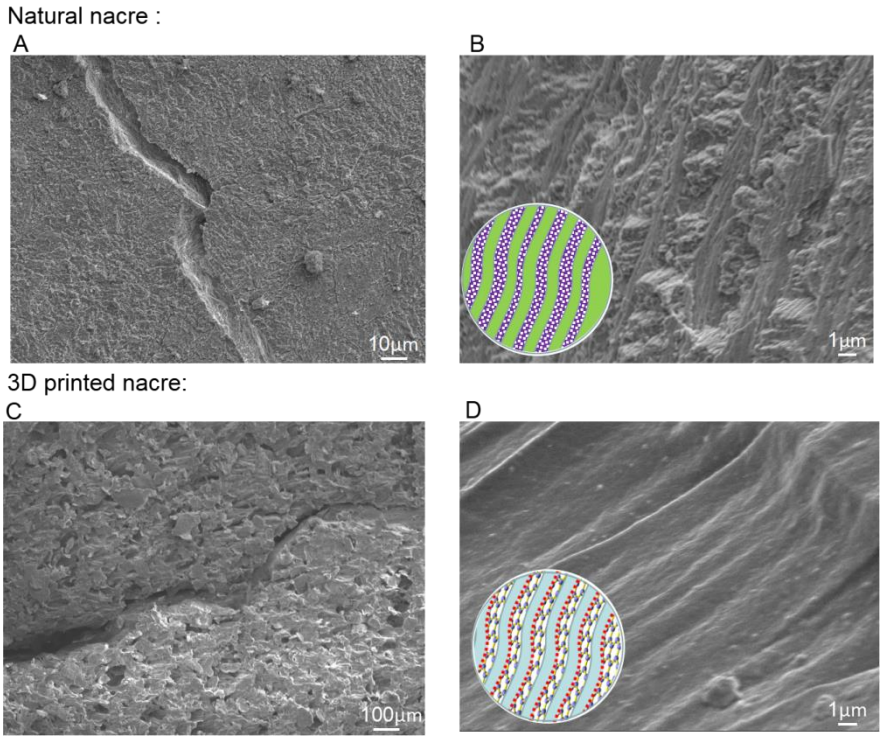

Fig. S9. Crack deflection and the brick-and-mortar structure in the natural nacre and the 3D-printed nacre. A comparison of crack deflection in the natural nacre (A) and the 3D-printed nacre (C). Schematic diagram shows the brick-and-mortar structure in the natural nacre (B) and the 3D-printed nacre (D).

Figure S10 shows the fracture of 3D-printed nacre after compression. Note that the crack is focused on the tip and propagates after the compression, which corresponds with the simulation results shown in fig. S10B. The natural nacre also shows a fracture on the tip after the compression (fig. S10C). Under loading, the weak hydrogen bonding in the GN-based artificial nacre is first ruptured and stretched along the sliding direction of graphene nanosheets, dissipating a large amount of energy. When the loading further increases, the π-π stacking between the polymer matrix and GN breaks. Then the strong covalent bonding between adjacent GNs as well as the network of polymer molecules will take the load, leading to the curving of the graphene nanoplatelets. The essence of the synergistic toughening effect is to simultaneously maximize the enhancement of the weak non-covalent and strong covalent bonding. Consequently, the mechanical properties of polymer/GNs nanocomposites are much improved [40].

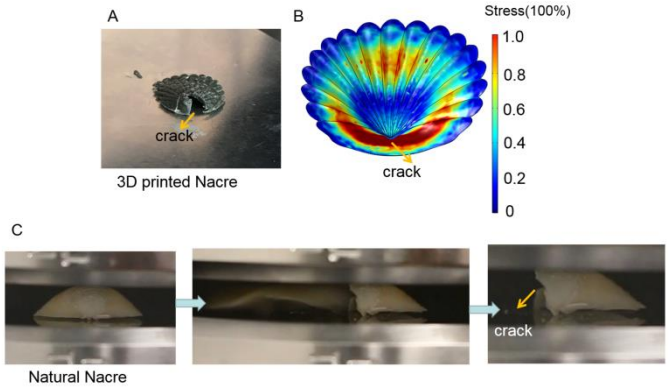

Fig. S10. A comparison of fracture behavior of the 3D-printed nacre and the natural nacre. (A) the 3D-printed nacre after failure; (B) simulation by Comsol Multiphysics shows the stress distribution of nacre model during compression; and (C) the break of natural nacre under compression. (Photo credit: Yang Yang, Epstein Department of Industrial and Systems Engineering, University of Southern California).

Droptower impact test:

The impact performance of the 3D-printed helmet was tested using a drop-tower instrument. Multiple specimens (a total of five) were tested at an incident velocity of 2.4 m/s. The tested specimens were fixed on a platform. In the impact test setup, the helmet (0.36g) exposed to the round impactor of 110 g in mass. The impactor dropped from a fixed height (h=0.3m) onto the clamped specimen. During the impact test, an LED was connected with the helmet to demonstrate the self-sensing of crack formation. After the impact test, the damage to the specimen was further analyzed for both random GNs (rGNs) and aGNs.

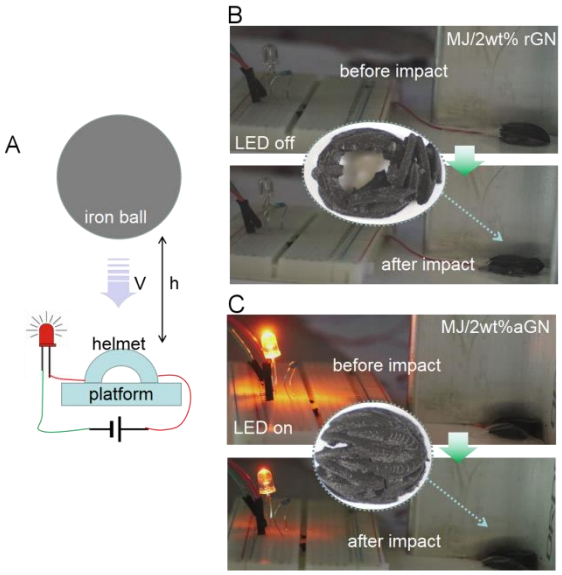

Fig. S11. The schematic diagram shows the drop-tower impact test setup for 3D printed helmet with rGNs and aGNs. The schematic diagram shows the drop-tower impact test setup (A) on 3D-printed helmets with rGNs (B) and aGNs (C). (Photo credit: Yang Yang, Epstein Department of Industrial and Systems Engineering, University of Southern California).

Flexural strength test:

For a rectangular sample under a load in a standard three-point-bending setup (without notch), the flexural strength will be : $\sigma = \frac{3FL}{2bd^2}$

in which *F* is the load at the fracture point, *L* is the length of the support span, *b* is the width, and *d* is the thickness of the sample. The test samples were fabricated by the developed electrically assisted 3D printing process. The MJ/rGNs samples were built without using electric field while the MJ/aGNs samples were created using the designed electric field. All of the samples were fabricated for 30 layers with a layer thickness of 50 μm. The widths of the samples are 3.5mm.

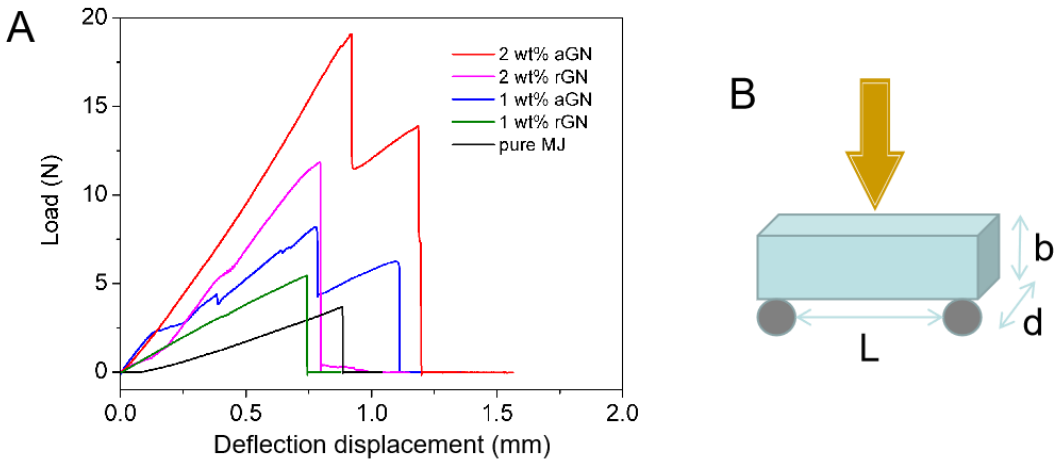

Fig. S12. The standard three-point bending tests were performed to study the flexural strength of the 3D-printed structures.

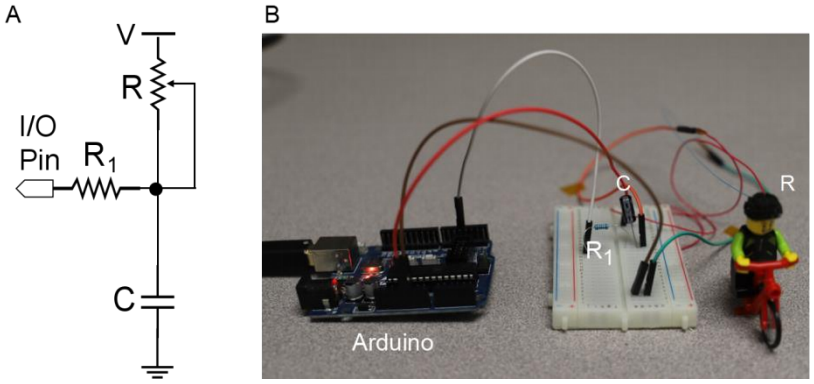

Fig. S13. The setup to test the resistance change of the 3D-printed helmet during compression. (Photo credit: Yang Yang, Epstein Department of Industrial and Systems Engineering, University of Southern California).

The setup to test the resistance change of the 3D-printed helmet during compression is shown in fig. S13. We used a micro-controller (Arduino) to measure the resistance change during the compression and the drop-tower impact. For the constructed RC circuit, we used an RCTIME function provided by the micro-controller to measure the resistance.

For the RC circuit, $\tau = RC$, $V_C = V(1-e^{-\frac{t}{\tau}})$, thus $\mathrm{R} = \frac{\tau}{C}$

The measured resistance changes during compression of the 3D-printed helmet for different loadings of rGNs and aGNs are shown in fig. S14.

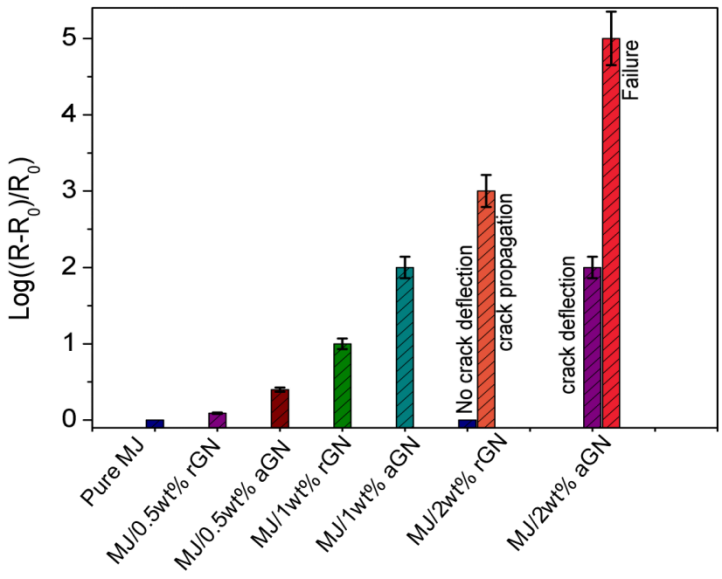

Fig. S14. A comparison of the resistance changes of the 3D-printed helmets with different loadings of rGNs and aGNs during compression.

Supplementary Discussion:

In our study, the volume fraction of graphene platelets is 1.06 vol% for 2wt%. The calculation is based on the density of photocurable resin (1.05 g/cm^3) and the density of graphene nanoplatelets (2g/cm^3). The loading of aGNs in the 3D-printed structures is not as high as the loading of $CaCO_3$ platelets in natural nacre; However, due to the large surface area (120-150 m^2/g), large diameter (25µm), and extremely thin thickness (~8nm) of GN, adjacent *GN* platelets after alignment are interconnected in the *XY* plane, and the polymer matrix between aGNs bonds them together to form the 'brick and mortar' architecture. As shown in fig. S15, the interconnected *aGN* on the surface are observed from the SEM image of the 3D-printed nacre. This interconnection forms a nacre-inspired 'brick and mortar' structure, in which GNs act as brick and the polymer matrix in between serves as mortar. For simplicity, the thickness of the Graphene nanoplatelet is ~8nm, for 1.06 vol% loading of aGNs, the thickness of the polymer is calculated to be ~0.75µm (fig. S15B). The gap distance is much smaller than the diameter of GN (25µm), making the strong bonding between different layers of GN. The large surface area and

surface modification of GN also make efficient load transfer between the polymer matrix and aGNs under loading. The schematic diagram in fig. S15B shows the crack propagation in composite with rGNs and crack deflection in composite with aGNs. Note that the interconnected layered aGNs leads to crack deflection. The 3D-printed nacre shows the 'brick and mortar' structure similar to that of the natural nacre with crack deflection behavior even with low loading of GNs. The small volume fraction also leads to the lightweight property (density 1.06g/cm^3 compared with 2.58 g/cm^3 for natural nacre), which is essential for applications such as wearable armors. The 3D-printed nacre with the loading of ~1vol% aGNs shows comparable specific toughness with the natural nacre, demonstrating promising applications of the developed electrically assisted 3D printing method.

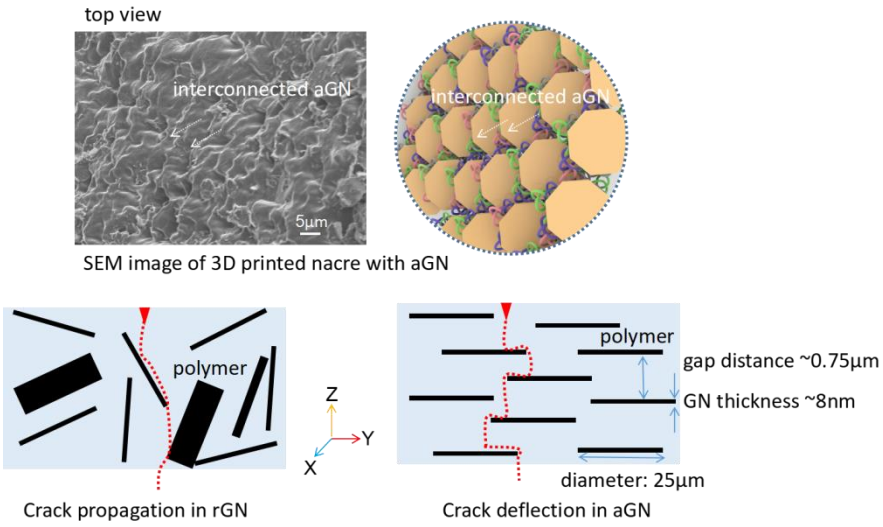

Fig. S15. Illustration of the microstructure of the 3D-printed nacre with rGNs and aGNs. (A) SEM image of the 3D printed nacre with aGNs shows the interconnected aGNs in the XY plane; and (B) schematic diagrams show the crack propagation in rGNs and aGNs.

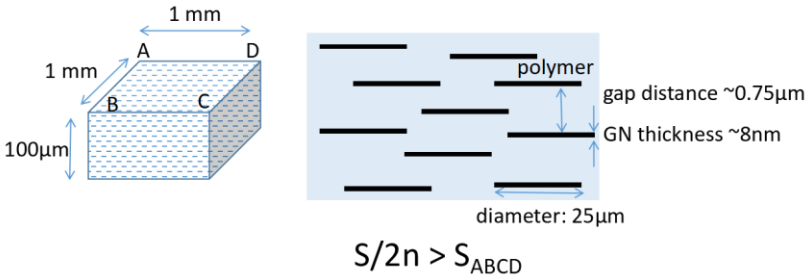

Fig. S16. The calculation of the interconnection of GNs in 3D-printed structures.

As shown in fig. S16, for simplicity, we used a cube with size 1mm×1mm×100µm to calculate the interconnection of aGNs in the 3D-printed structures. Considering the volume fraction ~1.06% of GNs and the thickness of a Graphene nanoplatelet (~8nm), the gap distance between parallelly aligned GNs is estimated to be 0.75µm. So there are approximately n=100/(0.75+0.008)=132 nanoplatelets in the cube sample with a thickness of 100µm. The mass of GNs in this sample is estimated to be $1.06 g/cm^3 \times V \times 2wt\% = 3.12 \times 10^{-6}$ g. As the surface area of GNs is 120-150 m^2/g, the total surface area of GNs in this sample is $S = 374.4 \times 10^{-6} \sim 468 \times 10^{-6}$ m^3. Since the surface area of the top surface is $S_{ABCD} = 1 \times 10^{-6} m^2$, $S/2n = 1.4 \times 10^{-6} \sim 1.75 \times 10^{-6}$ $m^2 > S_{ABCD}$ (fig. S16). Hence the interconnection of GNs in the *XY* plane for the 2wt% GNs loading exists in the 3D-printed nacre-inspired structure, which is in agreement with the SEM images shown in fig. S15.